Curious case of the maximum rigidity distribution
of cosmic-ray accelerators

D. Ehlert[1,*] F. Oikonomou[1] and M. Unger[2,1]

[1]*Institutt for fysikk, Norwegian University of Science and Technology (NTNU), 7491 Trondheim, Norway*
[2]*Institute for Astroparticle Physics, Karlsruhe Institute of Technology (KIT), 3640 Karlsruhe, Germany*

In many models, the sources of ultrahigh-energy cosmic rays (UHECRs) are assumed to accelerate particles to the same maximum energy. Motivated by the fact that candidate astrophysical accelerators exhibit a vast diversity in terms of their relevant properties such as luminosity, Lorentz factor, and magnetic field strength, we study the compatibility of a population of sources with nonidentical maximum cosmic-ray energies with the observed energy spectrum and composition of UHECRs at Earth. For this purpose, we compute the UHECR spectrum emerging from a population of sources with a power-law, or broken-power-law, distribution of maximum energies, applicable to a broad range of astrophysical scenarios. We find that the allowed source-to-source variance of the maximum energy must be small to describe the data if a power-law distribution is considered. Even in the most extreme scenario, with a very sharp cutoff of individual source spectra and negative redshift evolution of the accelerators, the maximum energies of 90% of sources must be identical within a factor of 3—in contrast to the variance expected for astrophysical sources. Substantial variance of the maximum energy in the source population is only possible if the maximum energies follow a broken-power-law distribution with a very steep spectrum above the break. However, in this scenario, the individual source energy spectra are required to be unusually hard with increasing energy output as a function of energy.

I. INTRODUCTION

Ultrahigh-energy cosmic rays (UHECRs) are charged particles that reach Earth with energies of up to several 10^{20} eV. The identification of the astrophysical sources capable of accelerating particles to these energies is one of the unsolved mysteries of high-energy astrophysics (see e.g. [1,2] for recent reviews). A correlation between astrophysical objects and the measured arrival directions of cosmic rays has not yet been established at high significance [3], but the source properties are constrained by measurements of the diffuse particle flux and composition at Earth; see e.g. [4–20].

Most of these studies assume an acceleration mechanism that is universal in rigidity[1] up to a maximum rigidity of $R_{\max}$, leading to consecutive flux suppressions of the elemental spectra at energies of $E_{\max} = ZR_{\max}$, where Z denotes the cosmic-ray charge. Assuming such a "Peters cycle" [21,22] at the sources gives a good description of the flux and composition measured at Earth at ultrahigh energies; see e.g. [11]. Depending on the source environment, the maximum energy can follow a different functional

form [23]. Here, we consider primarily the canonical scenario where the maximum energy scales in proportion to the nuclear charge and briefly discuss the effect of alternate scalings on our results.

A major caveat of many studies is that the sources are typically assumed to be identical—a description that is unlikely to hold for realistic sources. The most probable astrophysical candidates for the sources of UHECRs, e.g. active galactic nuclei (AGN) and gamma-ray bursts (GRBs), are generally not very similar—even within a single source class—but exhibit an enormous diversity in terms of key parameters like luminosity, size, magnetic field and jet power.

Only a few studies have relaxed the assumption of identical sources in the past, by focusing on a low number of discrete local sources [24–26] or by considering the superposition of a few (≤ 3) source classes, e.g. [15,18,20,27–29]. The time variation of $R_{\max}$ in AGN jets was studied in Ref. [30], and the effective spectrum produced by sources with nonidentical spectral shapes and spectral indices has been discussed in the context of gamma-ray spectra [31] and Galactic cosmic-ray sources [32]. Populations of sources with nonidentical maximum cosmic-ray rigidities were considered previously, for a pure proton UHECR composition [33], for Galactic cosmic rays [34], and for gamma-ray bursts [16].

---

*domenik.ehlert@ntnu.no
[1]The rigidity of a particle with charge Ze and momentum p is $R = pc/(Ze) \simeq E/Z$ (using natural units and with energy E).

Here we present, for the first time, a rigorous exploration of the population variance of R_{max} compatible with current observations of the spectrum and composition of UHECRs. This is achieved by convolving the distribution of source properties, parametrized by the maximum rigidity, with the individual source spectra to obtain an analytical description of the total population spectrum, as detailed in Sec. II. We simulate the propagation of UHECRs to Earth through the extragalactic photon fields and find the best source parameters by comparing the model predictions to UHECR data in Sec. III. From this, we derive lower limits on the source variance allowed by the data, as described in Sec. IV. We conclude in Sec. V that only a limited amount of population variance is permitted, and UHECR sources are required to be nearly identical in terms of maximum rigidity under realistic choices of the model parameters if a power-law distribution of maximum rigidities is assumed. The variance can be large for broken-power-law distributions, provided the source spectra are sufficiently hard. However, we find the distributions predicted for most candidate source classes—blazars, gamma-ray bursts, and tidal disruption events—to be incompatible with the limits obtained from the UHECR fit. Only sources with luminosity distribution similar to the one of Seyfert galaxies can potentially satisfy the constraints.

II. POPULATION SPECTRUM OF NONIDENTICAL SOURCES

In this study, we assume that the rigidity spectra of individual sources of UHECRs are well described by the aforementioned Peters cycle, and thus we assume a power law with a high-rigidity cutoff:

$$\phi_{src} = \frac{d^2N}{dRdt} = \sum_i \phi_0(Z_i)R^{-\gamma_{src}} f(R, R_{max}), \quad (1)$$

where the sum runs over all accelerated chemical elements with charge Z_i and the spectral index is assumed to be universal.[2] The term $f(R, R_{max})$ describes the high-rigidity cutoff at maximum rigidity R_{max}. We refer to the sum of the spectra of all sources within a certain volume as the population spectrum ϕ_{pop}.

In the limit of identical sources, the population spectrum will necessarily have the same shape as the spectra of individual sources. A source-by-source variation of the normalization factors $\phi_0(Z_i)$ does not lead to a qualitatively different population spectrum since it is equivalent to identical sources with the source-averaged normalizations ϕ_0, and thus we will not consider it in the following. It should, however, be kept in mind that the elemental fractions obtained from the fits presented later in this paper

should be understood as source-averaged fractions. A phenomenologically more interesting source property is the maximum rigidity. If the probability for an individual accelerator to reach a certain maximum rigidity is distributed as $p(R_{max}) \equiv dp/dR_{max}$ and the source spectra follow $\phi_{src}(R, R_{max})$, then the combined spectrum of the entire population is given by the convolution

$$\phi_{pop}(R) = \int_0^\infty \phi_{src}(R, R_{max})p(R_{max})dR_{max}. \quad (2)$$

Here and in subsequent occurrences of ϕ_{src}, the sum over all chemical elements of charge Z_i [cf. Eq. (1)] is assumed implicitly. In the following, we specify the functional forms of individual source spectra and probability distribution of R_{max} that will be studied in this work.

A. Source spectra

In general, the rigidity cutoff of astrophysical accelerators depends on the acceleration mechanism and the source environment, in particular on the dominant energy-loss process; see e.g. [37,38]. The simplest description of the shape is given by a sharp termination when particles exceed the maximum rigidity

$$\phi_{src}^{hs} = \phi_0 R^{-\gamma_{src}}\theta(R_{max} - R), \quad (3)$$

where $\theta(x)$ denotes the Heaviside step function. The population spectrum corresponding to this function has been studied previously in Ref. [33]. Since ϕ_{src}^{hs} describes the sharpest-possible rigidity cutoff, it provides a useful extreme case that will allow for a maximum variation of maximum rigidity among the sources in the population.

A more commonly used choice, expected under certain astrophysical conditions (see e.g. [38,39]), is given by an exponential cutoff

$$\phi_{src}^{exp} = \phi_0 R^{-\gamma_{src}} \exp\left(-\frac{R}{R_{max}}\right). \quad (4)$$

However, this function has the disadvantage that the effect of the cutoff already starts to become noticeable well below the maximum rigidity and the interpretation of the spectral index γ_{src} is complicated. For this reason, some phenomenological studies assume a broken-exponential source spectrum (e.g. [11]):

$$\phi_{src}^{b\text{-}exp} = \phi_0 R^{-\gamma_{src}} \begin{cases} 1 & R < R_{max}\exp \\ \left(1 - \frac{R}{R_{max}}\right) & \text{otherwise,} \end{cases} \quad (5)$$

which alleviates the issue but lacks physical motivation.

Finally, we consider spectra with an exponential cutoff raised to the power of λ_{cut}:

---

[2]$\gamma_{src} \approx 2$ for diffusive shock acceleration [35,36], but in this study the value of γ_{src} is a free parameter.
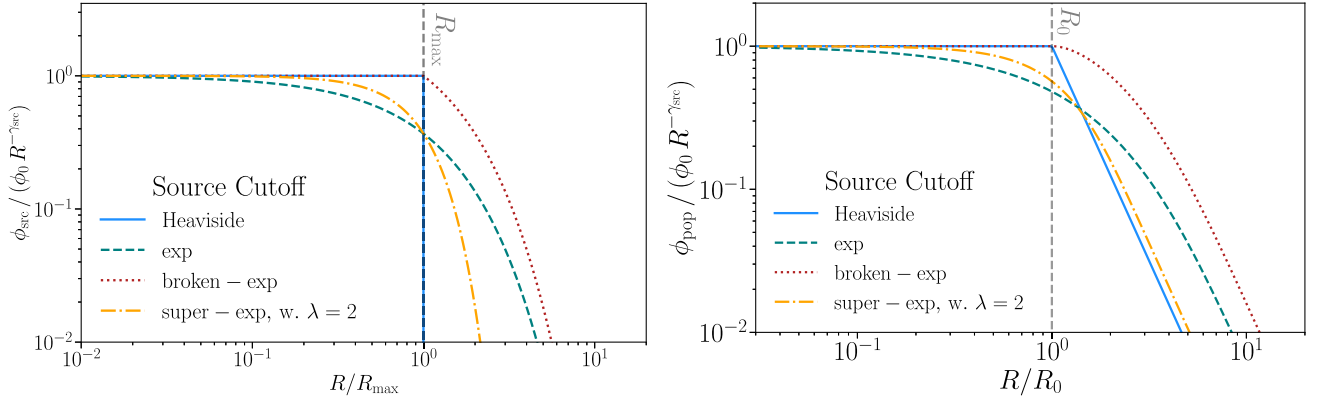
FIG. 1. Left: cosmic-ray source spectra for the different rigidity cutoff functions. R_{max} denotes the maximum rigidity and the y axis is scaled to show the ratio to an unmodified power law with spectral index γ_{src}. Right: population spectra resulting from the convolution of a power-law distribution of maximum rigidities above rigidity R_0 and the source spectra displayed in the left panel ($\beta_{pop} = 4$).

$$\phi_{src}^{s\text{-}exp} = \phi_0 R^{-\gamma_{src}} \exp\left(-\frac{R}{R_{max}}\right)^{\lambda_{cut}}, \qquad \lambda_{cut} > 0. \quad (6)$$

We refer to this description as a "superexponential" cutoff. The function can be used to interpolate continuously between classical, exponential cutoffs ($\lambda_{cut} = 1$) and sharp, Heaviside-like terminations ($\lambda_{cut} = \infty$). Additionally, for $\lambda_{cut} < 1$ the cutoff shape becomes subexponential up to no cutoff when $\lambda_{cut} \to 0$. Superexponential cutoff profiles were obtained e.g. in Ref. [39] with $\lambda_{cut} = 2$ for synchrotron losses during acceleration.

An illustration of the source spectrum for different choices of the cutoff is shown in the left panel of Fig. 1.

B. Distribution of maximum rigidities

1. Power law

In this paper, we mainly consider a population of sources with a distribution of maximum rigidities that follows a power law (PL) with spectral index β_{pop} above a minimum allowed maximum rigidity R_0:

$$p(R_{max}) = \begin{cases} 0 & R_{max} < R_0 \\ \frac{\beta_{pop}-1}{R_0}\left(\frac{R_{max}}{R_0}\right)^{-\beta_{pop}} & \text{otherwise,} \end{cases} \quad (7)$$

which is also known as a Pareto distribution. This R_{max} distribution was previously considered in Ref. [33]. Because of the asymmetric nature of the power-law distribution, the standard deviation is of limited use to characterize the source variance, and instead we will report the one-sided 90% quantile $R_{max}^{0.90}$ defined as

$$\int_{R_0}^{R_{max}^{0.90}} dR_{max}\, p(R_{max}) = 0.90. \quad (8)$$

For a power-law distribution of maximum rigidities, the quantile q is given by the relation

$$R_{max}^q/R_0 = [1-q]^{1/(1-\beta_{pop})}. \quad (9)$$

For illustration, population diversity of more than a decade, i.e. $R_{max}^{0.90}/R_0 \geq 10$, is obtained if $\beta_{pop} < 2$.

2. Broken power law

Alternatively, the distribution of maximum rigidities can be modeled as a broken power law (BPL) which can be written as

$$p(R_{max}) = \frac{R_0^{-1}}{C} \times \begin{cases} \left(\frac{R_{max}}{R_0}\right)^{-\beta_1} & R_{max} \leq R_0 \\ \left(\frac{R_{max}}{R_0}\right)^{-\beta_2} & R_{max} > R_0, \end{cases} \quad (10)$$

with C a normalization constant. A detailed discussion of the BPL scenario is provided in Appendix B.

C. Population spectrum

1. Power law

Assuming a power-law distribution of R_{max}, it is possible to derive an analytical description of the population spectrum for all source spectra presented in Sec. II A. In the case of sources with a Heaviside termination in rigidity, the population spectrum is given by

$$\phi_{pop}^{hs} = \phi_0 R^{-\gamma_{src}} \begin{cases} 1 & R < R_0 \\ \left(\frac{R}{R_0}\right)^{-\beta_{pop}+1} & \text{otherwise.} \end{cases} \quad (11)$$

For source spectra with a broken exponential cutoff, the population spectrum becomes

$$\phi_{pop}^{b\text{-}exp} = \phi_0 R^{-\gamma_{src}} \begin{cases} 1 & R < R_0 \\ \left(\frac{R}{R_0}\right)^{-\beta_{pop}+1} f\left(\frac{R}{R_0}, \beta_{pop}\right) & \text{otherwise} \end{cases} \quad (12)$$

with

$$f\left(\frac{R}{R_0}, \beta_{\text{pop}}\right) = 1 + e(\beta_{\text{pop}} - 1)$$

$$\times \left[\gamma\left(\beta_{\text{pop}} - 1, \frac{R}{R_0}\right) - \gamma(\beta_{\text{pop}} - 1, 1)\right].$$

Finally, for sources with a (super)exponential cutoff, the population spectrum is given by

$$\phi_{\text{pop}}^{\text{s-exp}} = \phi_0 R^{-\gamma_{\text{src}}} \left(\frac{R}{R_0}\right)^{-\beta_{\text{pop}}+1} \frac{\beta_{\text{pop}} - 1}{\lambda_{\text{cut}}}$$

$$\times \gamma\left(\frac{\beta_{\text{pop}} - 1}{\lambda_{\text{cut}}}, \left(\frac{R}{R_0}\right)^{\lambda_{\text{cut}}}\right). \qquad (13)$$

For a standard exponential distribution, i.e. $\lambda_{\text{cut}} = 1$, this simplifies to

$$\phi_{\text{pop}}^{\text{exp}} = \phi_0 R^{-\gamma_{\text{src}}} \left(\frac{R}{R_0}\right)^{-\beta_{\text{pop}}+1} (\beta_{\text{pop}} - 1) \times \gamma\left(\beta_{\text{pop}} - 1, \frac{R}{R_0}\right), \qquad (14)$$

whereas for $\lambda_{\text{cut}} \to \infty$, Eq. (11) is recovered. Here γ denotes the lower incomplete gamma function, not to be confused with the source spectral index γ_{src}.

Population spectra for a particular choice of parameters are shown in Fig. 1, right. The main impact of the cutoff parameter λ_{cut} is a later onset and faster turnover of the spectral break around R_0. The limiting behavior of the population spectrum is independent of the source cutoff function. The asymptotic rigidity dependencies of the population spectra are

$$\lim_{R \to 0} \phi_{\text{pop}}(R) \propto R^{-\gamma_{\text{src}}} \qquad (15)$$

and

$$\lim_{R \to \infty} \phi_{\text{pop}}(R) \propto R^{-\gamma_{\text{src}}-\beta_{\text{pop}}+1}. \qquad (16)$$

2. Broken power law

In the broken-power-law scenario, the resulting population spectrum for sources with superexponential cutoff is

$$\phi_{\text{pop}}^{\text{s-exp}} = \frac{\phi_0}{C \cdot \lambda_{\text{cut}}} R^{-\gamma_{\text{src}}} \times [L + H], \qquad (17)$$

with

$$L = \left(\frac{R}{R_0}\right)^{-\beta_1+1} \cdot \Gamma\left(\frac{\beta_1 - 1}{\lambda_{\text{cut}}}, \left(\frac{R}{R_0}\right)^{\lambda_{\text{cut}}}\right),$$

$$H = \left(\frac{R}{R_0}\right)^{-\beta_2+1} \cdot \gamma\left(\frac{\beta_2 - 1}{\lambda_{\text{cut}}}, \left(\frac{R}{R_0}\right)^{\lambda_{\text{cut}}}\right). \qquad (18)$$

Here "C" is a normalization factor (see Appendix B), "L" reflects the contribution from sources with $R_{\text{max}} \leq R_0$ and "H" represents sources above the break. Γ and γ are the upper and lower incomplete gamma function, respectively. The single-power-law scenario is retrieved as a limiting case of the more general broken-power-law case for $\beta_1 \to -\infty$, i.e. when the contribution L of low-R_{max} sources vanishes. We discuss the broken-power-law scenario in more detail in Appendix B. Here we only mention that the same expression for the population spectrum as in the power-law picture holds approximately after defining the effective spectral index $\gamma_{\text{pop}} = \gamma_{\text{src}} + \beta_1 - 1$ and R_{max}-distribution index $\beta_{\text{pop}} = \beta_2 - \beta_1 + 1$.

D. Relation to astrophysical quantities

The population spectra derived in the previous section provide simple analytic expressions that are well suited for fits to UHECR observations at Earth, with which the key parameters β_{pop} and γ_{src} can be derived. The connection of these parameters to the properties of UHECR sources is discussed in the following for a few examples. We will show that the assumed power-law distribution in maximum rigidity can be attributed to different acceleration scenarios.

TABLE I. Summary of parameters used for the three illustrative scenarios. See sections given in the first column for further details.

Scenario	Parameter	Description	Equation
Power law (Section II B)	γ_{src}	True spectral index of the sources	$\phi_{\text{src}} \propto R^{-\gamma_{\text{src}}}$
	γ_{pop}	Effective spectral index of the sources [same as the true spectral index for a power-law distribution of $p(R_{\text{max}})$]	$\phi_{\text{pop}} \propto R^{-\gamma_{\text{pop}}}$
	β_{pop}	(Effective) spectral index of the $p(R_{\text{max}})$ distribution	$p(R_{\text{max}}) \propto R_{\text{max}}^{-\beta_{\text{pop}}}$
	β_1, β_2	Spectral index of the distribution of maximum rigidities below (above) the break for a broken power law in $p(R_{\text{max}})$	$p(R_{\text{max}}) \propto R_{\text{max}}^{-\beta_1}(R_{\text{max}}^{-\beta_2})$
Lorentz factor (Section II D 1)	η	Spectral index of the power-law distribution of Lorentz factors	$dp/d\Gamma \propto \Gamma^{-\eta}$
	α	Energy boosting by the relativistic motion of the jet	$E = E'\Gamma^{\alpha}$
	ξ	Time dilation caused by the relativistic motion of the source region	$t = t'\Gamma^{\xi}$
Luminosity (Section II D 2)	y_1, y_2	Spectral index of the broken-power-law luminosity function of sources below (above) the break	$dp/dL \propto L^{-y_1}(L^{-y_2})$

TABLE II.   Effective fit parameters, β_{pop}, the spectral index of the maximum rigidity distribution of the UHECR source population, γ_{src}, the assumed spectral index of the UHECR spectrum of individual sources, and their interpretation in terms of source properties for various scenarios considered in this work. The scenarios are (I) a distribution of $p(R_{\mathrm{max}})$ that follows an *ad hoc* single PL or BPL; (II) maximum rigidity that scales as $R_{\mathrm{max}} \propto \Gamma^{\alpha}$ with Γ the PL-distributed bulk Lorentz factor of the acceleration region (see Sec. II D 1) with $\mathrm{d}p/\mathrm{d}\Gamma \propto \Gamma^{-\eta}$; and (III) R_{max} as a function of source luminosity, $R_{\mathrm{max}} \propto \sqrt{L}$, with PL or BPL distribution of $\mathrm{d}p/\mathrm{d}L$ (see Sec. II D 2). For power-law distributions the parameter in brackets denotes the slope, e.g. $\mathrm{d}p/\mathrm{d}\Gamma(\eta) \propto \Gamma^{-\eta}$, while for broken-power-law distributions the parameters give the slope before and after the break, respectively. Scenario I represents our baseline model that we use to compute the population spectra for different source spectral cutoff functions. Cases II and III can be reduced to the former after reinterpretation of the source and population parameters (η, α, y_1, y_2, β_1, β_2, and γ_{src}) in terms of the parameters $\beta_{\mathrm{pop,max}}$ and γ_{pop}. For scenario III we quote the slopes for $\mathrm{d}p/\mathrm{d}L$, as opposed to $\mathrm{d}p/\mathrm{d}\log(L)$ which is often used in the literature. This introduces a factor of L^{-1}, i.e. $y_{1/2} \to y_{1/2} + 1$.

ID	Parameter	Distribution	β_{pop}	γ_{pop}	Sources	$\beta_{\mathrm{pop,max}}$
I. 1	R_{max}	PL, $p(R_{\mathrm{max}}\|\beta_{\mathrm{pop}})$	β_{pop}	γ_{src}		
I. 2	R_{max}	BPL, $p(R_{\mathrm{max}}\|\beta_1,\beta_2)$				
		$\beta_1 < 1$	$\approx \beta_2$	$\approx \gamma_{\mathrm{src}}$		
		$\beta_1 > 1$	$\beta_2 - \beta_1 + 1$	$\gamma_{\mathrm{src}} + \beta_1 - 1$		
II	$R_{\mathrm{max}} \propto \Gamma^{\alpha}$	PL, $\mathrm{d}p/\mathrm{d}\Gamma(\eta)$	$(\eta-1)/\alpha + 2$	γ_{src}	Blazars [40]$^{\mathrm{a}}$: $\eta = 1.4_{\pm 0.2}$	
			$-\gamma_{\mathrm{src}} + \xi/\alpha$		+ Hillas: $\alpha = 1$, $\xi = 1$	$3.4_{\pm 0.2} - \gamma_{\mathrm{src}}$
					+ Espresso: $\alpha = 2$, $\xi = 0$	$2.2_{\pm 0.1} - \gamma_{\mathrm{src}}$
III. 1	$R_{\mathrm{max}} \propto \sqrt{L}$	PL, $\mathrm{d}p/\mathrm{d}L(y_2)$	$2y_2 - 3$	γ_{src}	BL Lacs [41]$^{\mathrm{b}}$: $y_2 = 2.61_{\pm 0.37}$	$2.22_{\pm 0.74}$
					FSRQs [42]$^{\mathrm{b}}$: $y_2 = 2.36_{\pm 0.10}$	$1.72_{\pm 0.20}$
					Blazars [42]$^{\mathrm{b}}$: $y_2 = 2.32_{\pm 0.08}$	$1.64_{\pm 0.16}$
					TDEs [43,44]: $y_2 = 2.30_{\pm 0.20}$	$1.60_{\pm 0.40}$
III. 2	$R_{\mathrm{max}} \propto \sqrt{L}$	BPL, $\mathrm{d}p/\mathrm{d}L(y_1,y_2)$				
		$y_1 < 2$	$\approx 2y_2 - 3$	$\approx \gamma_{\mathrm{src}}$	GRBs [45]: $y_1 = 1.2_{-0.1}^{+0.2}$, $y_2 = 2.4_{-0.6}^{+0.3}$	$1.8_{-1.2}^{+0.6}$
					FSRQs [42]$^{\mathrm{b}}$: $y_1 = 0_{\pm 2.07}$, $y_2 = 2.67_{\pm 0.17}$	$2.34_{\pm 0.34}$
					Blazars [42]$^{\mathrm{b}}$: $y_1 = 0.49_{\pm 1.15}$, $y_2 = 2.79_{\pm 0.19}$	$2.58_{\pm 0.38}$
					Seyferts [46]: $y_1 = 1.96_{\pm 0.04}$, $y_2 = 3.71_{\pm 0.09}$	$4.42_{\pm 0.18}$

$^{\mathrm{a}}$A steeper distribution of $\eta = 2.1 \pm 0.4$ was found in [47] when fitting only blazars with $\Gamma = 1$–40, resulting in reduced population variance of $\beta_{\mathrm{pop}} = 4.1 \pm 0.4$ for the Hillas and $\beta_{\mathrm{pop}} = 2.6 \pm 0.2$ for the espresso scenario.
$^{\mathrm{b}}$Assuming the pure-luminosity-evolution (s/m) PLE model.

The relevant parameters of these scenarios are summarized in Table I and the reinterpretation of the fitted parameters β_{pop} and γ_{src} in terms of proposed underlying physical properties are listed in Table II. Through the reinterpretation of the fitted parameters, all considered physical scenarios can be reduced to the same population spectra that are obtained for a power-law distribution of R_{max}. The process is illustrated in Fig. 2.

1. Jet Lorentz factor

In some scenarios, for sources with relativistic jets, the maximum rigidity is directly related to the bulk Lorentz factor of the motion, Γ_{jet}. For instance, the Hillas criterion [48] for relativistic sources gives $R_{\mathrm{max}} = R_0 \Gamma_{\mathrm{jet}}$, with $R_0 \propto lB$, where l is the size of the source and B the magnetic field.

It is also possible that UHECRs are galactic cosmic rays that receive a "one-shot" boost of a factor of $\sim \Gamma_{\mathrm{jet}}^2$ in the jet of their host galaxies, in which case $R_{\mathrm{max}} \sim R_0 \Gamma_{\mathrm{jet}}^2$, where R_0 is the maximum energy of the cosmic rays before reacceleration. This is referred to as the *espresso*

mechanism [49–51]. Cosmic rays that do not enter the most relativistic parts of the jet are only partially boosted with $R_{\mathrm{max}} \propto \Gamma_{\mathrm{jet}}^{\alpha}, \alpha < 2$. Thus, here we investigate the general case of

$$R_{\mathrm{max}} = R_0 \Gamma_{\mathrm{jet}}^{\alpha}, \qquad (19)$$

where the aforementioned cases are described by $\alpha = 1$ (Hillas) and $\alpha \leq 2$ (espresso).

Assuming, for example, a power-law distribution of the Lorentz factors, as found consistent with observations of jetted AGN in Refs. [40,52],

$$\frac{\mathrm{d}p}{\mathrm{d}\Gamma_{\mathrm{jet}}} = (\eta - 1)\Gamma_{\mathrm{jet}}^{-\eta}, \qquad (20)$$

the distribution of maximum rigidities can be calculated as

$$\begin{aligned} p(R_{\mathrm{max}}) &= \frac{\mathrm{d}p}{\mathrm{d}\Gamma_{\mathrm{jet}}} \left| \frac{\mathrm{d}\Gamma_{\mathrm{jet}}}{\mathrm{d}R_{\mathrm{max}}} \right| \\ &= \frac{\eta - 1}{\alpha} R_0^{-1} \left(\frac{R_{\mathrm{max}}}{R_0} \right)^{\frac{1-\eta}{\alpha}-1} \theta(R_{\mathrm{max}} - R_0). \end{aligned} \qquad (21)$$
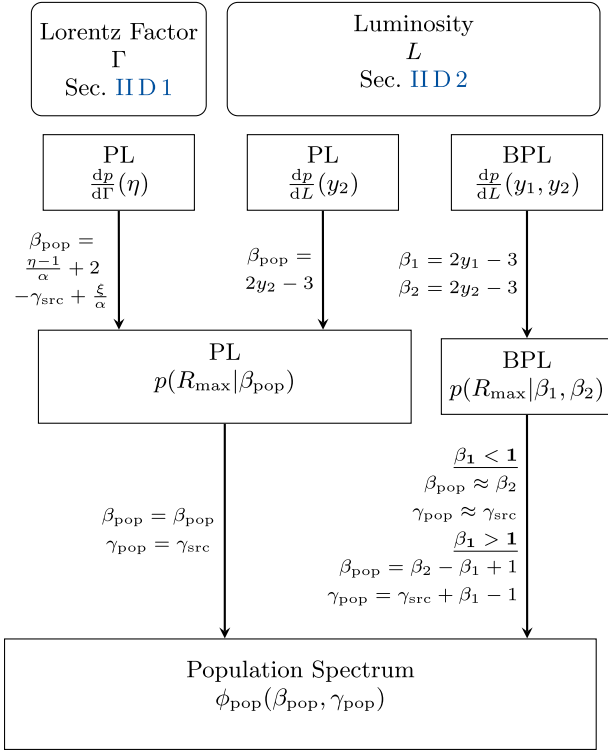
FIG. 2. Schematic description of how the parameters of the considered astrophysical scenarios (η, α, ξ, y_1, y_2, β_1, β_2, and $\gamma_{\rm src}$) are connected to the parameters ($\beta_{\rm pop}$ and $\gamma_{\rm pop}$) that describe the effective population spectrum $\phi_{\rm pop}$. In the first step, the single-PL or BPL distributions of physical parameters are converted to a PL or BPL distribution of maximum rigidities. This conversion is exact, assuming that Eqs. (19) and (24) are valid. If $R_{\rm max}$ follows a PL distribution, with slope $R_{\rm max}^{-\beta_{\rm pop}}$ above the threshold at R_0, we obtain our default case for the population spectrum. If $R_{\rm max}$ is distributed according to a broken power law, with break at R_T and slope $R_{\rm max}^{-\beta_1}/R_{\rm max}^{-\beta_2}$ before or after the break, the same parametrization of $\phi_{\rm pop}$ is possible but only after a reinterpretation of the parameters. This approach is exact except around the break at R_0.

Of course, R_0 is also expected to vary from source to source, and therefore the distribution of $R_{\rm max}$ should be broader and the above equation can be understood as a lower limit on the source-to-source variation of $R_{\rm max}$.

The boosting of particle energies also affects the expected flux emitted by individual sources. This introduces additional terms into Eq. (21) but we show in Appendix A that the convolution of the source spectra and the $R_{\rm max}$ distribution lead to the same functional forms as derived in the last section. However, the parameter $\beta_{\rm pop}$ can now be related to physical properties of the source population, namely the spectral index $\gamma_{\rm src}$, the Lorentz-boosting factor $R_{\rm max} \propto \Gamma_{\rm jet}^{\alpha}$, and the distribution of Lorentz factors $p(\Gamma_{\rm jet}) \propto \Gamma_{\rm jet}^{-\eta}$ via

$$\beta_{\rm pop} = \frac{\eta - 1}{\alpha} + 2 - \gamma_{\rm src} + \xi/\alpha, \tag{22}$$

where the time dilation factor $\xi = 1$ for an acceleration region comoving with the jet and $\xi = 0$ for espresso-type reacceleration.

2. Luminosity

Another plausible distribution of the maximum rigidity can be derived from the minimum luminosity requirement for particle acceleration in expanding flows. Here, the minimum luminosity L_0 needed to accelerate CRs to maximum rigidity R_0 is given by[3] [53–59]

$$L_0 \approx 10^{45.5} \frac{1}{\beta} \left(\frac{R_0}{10^{20}\ {\rm V}} \right)^2\ {\rm erg\ s^{-1}}, \tag{23}$$

where β is the speed of the flow in units of c. In this scenario, we can relate $R_{\rm max}$ and observed luminosity L of a source via

$$R_{\rm max} \sim R_0 \beta^{1/2} \left(\frac{L}{L_0} \right)^{1/2}. \tag{24}$$

The impact of the variance of β in a population can be approximately neglected for highly as well as mildly and nonrelativistic sources.[4]

In this scenario, where we relate the maximum rigidity to the source luminosity,

$$p(R_{\rm max}|z) = \frac{{\rm d}p}{{\rm d}L}(z) \left| \frac{{\rm d}L}{{\rm d}R_{\rm max}} \right|, \tag{25}$$

where ${\rm d}p(z)/{\rm d}L$ is the luminosity function of the sources. For a single-power-law distribution of luminosities, which can adequately describe many proposed source classes, and without taking into account the redshift evolution,[5] we can write

$$\frac{{\rm d}p}{{\rm d}L} = \frac{y_2 - 1}{L_0} \left(\frac{L}{L_0} \right)^{-y_2}. \tag{26}$$

---

[3]The normalization value varies slightly between different papers.

[4]If the acceleration region is highly relativistic, then $\beta \sim 1$ and there is no additional variance introduced by the nonidentical outflow speeds. Even in non- or mildly relativistic source environments, the impact is expected to be small. For example, the authors of [60] found that the relation between luminosity and outflow speed in a sample of AGN outflows is $L \sim v_{\rm out}^{4.6}$. The additional contribution in Eq. (24) is thus $\beta^{1/2} \sim L^{1/9}$, which constitutes only a subdominant effect compared to the original $R_{\rm max} \propto L^{1/2}$.

[5]For our purposes, luminosity and density redshift evolution of sources are indistinguishable in terms of the total contribution to the observed UHECR energy flux. However, as the maximum rigidity is related to the source luminosity [Eq. (24)], an evolution of maximum rigidities, $L(z) \to R_{\rm max}(z)$, would be introduced. The impact of such an evolution is studied in Sec. IV D, where we find that the cosmic-ray fit is not very sensitive to this behavior but negative evolutions, i.e. $R_{\rm max} \propto z^{\zeta}, \zeta < 0$, are preferred at moderate significance.

We assume that the emitted flux of a single source scales with the luminosity as $\phi_{\mathrm{src}} \propto L/L_0$. Noting Eq. (24), this introduces an additional dependency of the source flux on the maximum rigidity, which can be absorbed into the $p(R_{\mathrm{max}})$ distribution by adjusting the definition of the effective slope β_{pop}. The distribution of maximum rigidities is then

$$p(R_{\mathrm{max}}) = \frac{2(y_2 - 1)}{R_0} \left(\frac{R_{\mathrm{max}}}{R_0} \right)^{-2y_2 + 3}, \quad (27)$$

which, except for an additional normalization constant κ, reduces to the PL expression in Eq. (7) after defining

$$\beta_{\mathrm{pop}} = 2y_2 - 3 \quad \text{and} \quad \kappa = \frac{\beta_{\mathrm{pop}} + 1}{\beta_{\mathrm{pop}} - 1}. \quad (28)$$

The situation is more complex if sources follow a broken-power-law luminosity function $\mathrm{d}p/\mathrm{d}L(y_1, y_2)$. By defining $\beta_1 = 2y_1 - 3$ and $\beta_2 = 2y_2 - 3$, it is possible to express the maximum rigidity distribution as a broken power law.

The expected values of β_{pop} (labeled $\beta_{\mathrm{pop,max}}$) are listed in the last column of Table II for a selection of possible source candidates. These can be compared directly to the fitted values of β_{pop} discussed below. For the investigated sources $\beta_{\mathrm{pop,max}}$ is in general low, meaning that we would expect to observe the effect of the variance of the population in the UHECR data. It should be kept in mind that the estimates given in this section are only a lower limit on the source variance (upper limit on β_{pop}) as we focused only on the variation of a few key parameters and treated others as a constant (e.g. R_0) and therefore the real source variance will be larger. In addition, for sources observing a broken-power-law distribution the variance predicted from Eq. (8) with the tabled β_{pop} will underestimate the true population variance since only sources above the break are considered if the approximation as a single power law is made (case III. 2 of Table II). Depending on the distribution of sources below the break, the true variance can be much larger if β_1 is not small. The discrepancy is smaller if the subbreak distribution is inverted ($\beta_1 < 0$) and approaches zero for $\beta_1 \to -\infty$, in which case the expression reduces to a single power law [Eq. (7)].

III. METHODS

A. UHECR data

We use the latest publicly available data from the Pierre Auger Observatory for comparison with our numerical simulations. These are the energy spectrum of UHECRs from Ref. [61] and the mean and standard deviation of the maximum depth of air showers [62,63] that are sensitive to the composition of cosmic rays; see e.g. [64].

B. UHECR propagation

UHECR injection and propagation are simulated with the numerical Monte Carlo framework CRPropa3 [65], including the production of cosmogenic neutrinos and gamma rays. Upper limits and measurements of the latter are qualitatively taken into account in what follows. These are the Fermi-LAT isotropic diffuse gamma-ray background [66], the observed IceCube high-energy starting-event neutrino flux [67], and the IceCube 90% upper limits above 5×10^6 GeV [68]. The UHECR sources are simulated in the continuous-source approximation out to maximum redshift $z_{\mathrm{max}} = 4$. For UHECRs in the energy range that we fit, the effective horizon is much closer at no more than $z \lesssim 1$ (e.g. [69]), but sources at larger distances can have a strong impact on the predicted flux of cosmogenic neutrinos.

All relevant interactions are taken into account during propagation [11,65,70]; these are (i) redshift energy loss, (ii) photopion production, and (iii) electron-positron pair production on the cosmic microwave background (CMB) and the infrared background (IRB) [71], and for heavier cosmic rays also (iv) photodisintegration on CMB and IRB and (v) nuclear decay.

We assume that UHECRs propagate in the ballistic regime and neglect the effects of extragalactic magnetic fields on the trajectories of UHECRs. Based on the results of previous studies [29,72–76], these propagation effects are mainly important at low rigidities, where they can lead e.g. to an apparent hardening of the UHECR flux at Earth, but are not expected to alter our conclusions about the source variance of maximum rigidities.

C. Model fit

We compare the model-predicted UHECR spectrum and composition after propagation to observations by the Pierre Auger Observatory. For that purpose we convert the model composition into the air shower observables—the mean depth of the shower maximum $\langle X_{\mathrm{max}} \rangle$ and its standard deviation $\sigma(X_{\mathrm{max}})$—following Ref. [77].

The agreement between simulation and observations is evaluated with a standard χ^2 estimator plus additional penalty terms

$$\chi^2 = \sum_{E_i \geq E_{\mathrm{min}}} \left(\frac{d_i - m(E_i, \mathbf{p})}{\sigma_{\mathrm{stat}}(d_i)} \right)^2 + \chi_{\mathrm{UL}}^2 + \chi_{\mathrm{zero}}^2 + \chi_{\mathrm{shifts}}^2 \quad (29)$$

and minimized adjusting the model parameters $\mathbf{p}$. The sum runs over all Auger data points at energies E_i above the threshold energy. Here, d_i denotes the three measured quantities, i.e. the energy spectrum, average X_{max} and standard deviation of X_{max}. We select a high value of $E_{\mathrm{min}} = 10^{18.8}$ eV as the minimum fitted UHECR energy to reduce the impact of a possible low-energy cosmic-ray component, different from the one responsible for the

highest energies (Hillas' "component B" [78]). We have verified that the results are consistent within uncertainties under small changes of $E_{\min}$.

The smallest set of free fit parameters **p** are the minimum rigidity R_0 and slope β_{pop} of the single-power-law distribution of maximum rigidities, source spectral index γ_{src}, total population emissivity L_0, and elemental injection fractions f_A^R which are defined as relative flux ratios at the same rigidity.[6] A combination of five injection elements—^{1}H, ^{4}He, ^{14}N, ^{28}Si and ^{56}Fe—is used as an effective approximation of mass groups in the cosmic-ray composition.

For alternative "interaction limited" scenarios (e.g. [23]), a scaling of the maximum energy with the CR mass is typically predicted. Yet, for most stable injection elements, except hydrogen, there is an approximately constant relation between CR mass and charge, with $A/Z \approx 2$, and the transition from $E_{\max} \propto Z$ to $E_{\max} \propto A$ would thus only result in a rescaling of the reference rigidity R_0 by a constant factor. For proton injection, where $A/Z \neq 2$, the maximum energy will not follow the same linear scaling but will be offset by a relative factor of $(A/Z)_{\mathrm{p}}/(A/Z)_{\mathrm{elem}\neq\mathrm{p}}$. However, since in our fits this component consistently sits below the ankle, the impact on the results is expected to be negligible.

We treat spectral data points below the threshold as one-sided χ^2 penalty terms that only contribute to the overall goodness of fit if the predicted flux exceeds the observations. This component is denoted as χ^2_{UL} in Eq. (29) and is analogous to the first term but only evaluated if the model exceeds the data.

No cosmic rays were observed in the two highest-energy bins at $E \geq 10^{20.2}$ eV and only 90% upper limits are given in [61]. The χ^2 penalty derived for this type of zero-event data points follows from the asymptotic χ^2 term assuming a Poissonian distribution of events [79] and is estimated as

$$\chi^2_{\mathrm{zero}} = \sum_{i=1}^{\mathrm{ULs}} 2 n_i^{\mathrm{model}}, \tag{30}$$

where n_i^{model} is the number of particles predicted by the simulation at the energy $E(\mathrm{UL}_i)$ after taking into account the detector exposure [61].

Finally, we consider the systematic uncertainties in the absolute scale of the energy, $\langle X_{\max} \rangle$ and $\sigma(X_{\max})$. They are included in the fit as nuisance parameters with

$$\chi^2_{\mathrm{shifts}} = \sum_{k \in \{E, \langle X_{\max}\rangle, \sigma(X_{\max})\}} \left(\frac{\delta_k}{\sigma_k}\right)^2, \tag{31}$$

where the energy uncertainty is assumed as $\sigma_E \leq 14\%$ [80] and the shower depth uncertainties are taken directly from

---

[6]Fractions are sometimes defined at the same energy instead of rigidity. A transformation between the two parametrizations can be achieved via $f_A^R = f_A^E \cdot Z(A)^{-\gamma_{\mathrm{src}}+1}$.

the dataset [62,63]. The scale shifts can be fitted freely in the range $\delta_k \in [-\sigma_k, \sigma_k]$, but unless indicated otherwise, we fix the values of the systematic shifts δ_k to fiducial values, as detailed below.

IV. RESULTS AND DISCUSSION

A. Fiducial model

The observed variance of $X_{\max}$ consists of two separate contributions: (i) shower-to-shower variations and (ii) intrinsic shower variability. To allow for stronger source diversity, it is necessary that $\sigma(X_{\max})$ is not already dominated by the latter. Air showers originating from light primary cosmic rays have a larger variability [77], and intrinsic shower variations are minimized by shifting the observational data to the heaviest composition that is allowed within systematic uncertainties—corresponding to an adjustment of $\langle X_{\max} \rangle$ by about -8.5 g cm^{-2} at the ankle and -7 g cm^{-2} at the highest energies [62,63]. In addition, we shift the observed variance of the shower maximum up by the systematic uncertainty to allow for the largest reasonable source variance. We adopt these shifts as our fiducial model to allow for maximum intrinsic source diversity. An adjustment of the energy scale is also possible, but we found our conclusions to be invariant under such a shift and neglect it for simplicity.

We furthermore select Sibyll2.3c [81] as our default hadronic interaction model to convert the predicted UHECR composition to mean shower depth and variance. This is motivated by the fact that interpreting the $X_{\max}$ data

TABLE III. Best-fit parameters for several variations of the source model. From left to right: the base scenario with Sibyll2.3c as air shower model and no shifts of the energy and $X_{\max}$ scales of the data; our fiducial model, Sibyll2.3c and the $\langle X_{\max} \rangle$ [$\sigma(X_{\max})$] data points shifted by -1 ($+1\sigma_{\mathrm{syst}}$), respectively; the same scale shifts but with Epos-LHC as air shower model. The injection fractions are given in descending order for p, He, N, Si and Fe. An asterisk indicates that the confidence interval extends to the edge of the scan range and the parameter is not properly constrained in that direction.

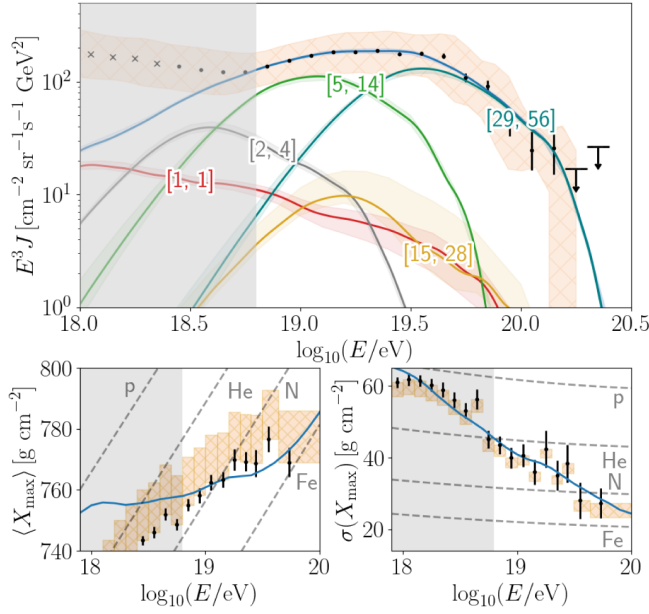| Model	Sibyll2.3c (no shifts)	Sibyll2.3c (fiducial shifts)	Epos-LHC (fid. shifts)
R_0 [EV]	$1.73^{+0.20}_{-0.18}$	$0.57^{+1.88}_{-0.11}$	$1.6^{+0.6}_{-0.4}$
β_{pop}	$29.9^{+1.7*}_{-18.1}$	$5.2^{+26.4*}_{-0.5}$	$4.4^{+0.5}_{-0.5}$
γ_{src}	$-0.23^{+0.18}_{-0.26}$	$-0.8^{+1.4}_{-0.5}$	$0.1^{+0.4}_{-0.5}$
$f_A^R[\%]$	0^{+0}_{-0}	$0^{+36.4}_{-0}$	0^{+0}_{-0}
	$58.1^{+0.4}_{-1.9}$	$0^{+51.3}_{-0}$	$36.9^{+7.4}_{-22.8}$
	$35.0^{+1.6}_{-0.2}$	$93.7^{+0.5}_{-53.5}$	$50.3^{+16.3}_{-5.4}$
	$5.7^{+0.5}_{-0.6}$	$0.3^{+7.7}_{-0.3}$	$11.3^{+6.6}_{-3.8}$
	$1.16^{+0.12}_{-0.11}$	$6.0^{+0.2}_{-3.8}$	$1.41^{+0.27}_{-0.04}$
$R_{\max}^{0.90}$ [R_0]	$1.083^{+0.155}_{-0.005}$	$1.72^{+0.13}_{-0.64}$	$1.97^{+0.22}_{-0.17}$
$\chi^2/\mathrm{d.o.f.}$	$45.0/26$	$40.4/26$	$56.3/26$

FIG. 3.   Predicted spectrum and composition at Earth for the best-fit scenario of the fiducial model [Sibyll2.3c, $\langle X_{\max} \rangle - \sigma_{\text{syst}}$, $\sigma(X_{\max}) + \sigma_{\text{syst}}$]. The colored bands indicate the contributions of the separate mass groups with $[A_{\min}, A_{\max}]$, including the 68% uncertainties (1 d.o.f.). Hatched areas indicate systematic uncertainties of the data. Data points at $E < 10^{18.4}$ eV (crosses) are taken from [83] and are only shown for visual guidance. Only points above $10^{18.8}$ eV are used in the fit.
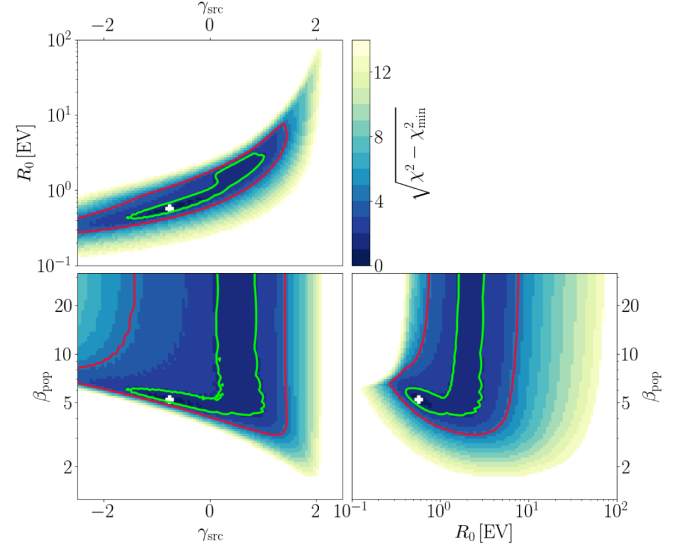

FIG. 4.   Results of the source parameter scan for the fiducial model marginalized along all but two axes respectively. The surface plot shows the agreement between prediction and Auger observations in terms of the χ^2 estimator and the contour lines indicate the one (green) and three (red) sigma confidence interval for two degrees of freedom. The best fit is marked with a white cross.

of Auger with Sibyll yields a heavier composition than when using Epos-LHC [82]. As default, we assume a flat redshift evolution of the source density and an exponential source cutoff. Alternative redshift evolutions are explored in Sec. IV C and different cutoff functions in Sec. IV E.

In line with our outlined considerations, we find that the fiducial scale shifts allow for increased population variance compared to the unshifted observations, as shown in Table III. This is true independent of the choice of hadronic interaction model.

The predicted spectrum and composition at Earth for the best-fit source parameters of the fiducial model are shown in Fig. 3. The viable range of β_{pop} is sharply bounded from below (Fig. 4), approximately as

$$\beta_{\text{pop}} \gtrsim -\gamma_{\text{src}} + 4, \tag{32}$$

and appreciable source diversity is only possible for soft source spectra $\gamma_{\text{src}} \gtrsim 1$. Yet, when assuming acceleration following a Peters cycle, soft source spectra imply a significant amount of mixing between the different mass groups, which leads to an increase in shower variance, a prediction that is in tension to the low values of $\sigma(X_{\max})$ measured by the Pierre Auger Collaboration, and the resulting agreement between simulation and observations is poor. This problem is exacerbated for the soft spectra

expected from diffusive shock acceleration, and values above $\gamma_{\text{src}} \approx 2$ are excluded.

Realizations of the source model where Eq. (32) is violated are characterized by a population spectrum with an extreme UHE tail, a consequence of $\lim_{R \to \infty}(\phi_{\text{pop}}) \propto R^{-\beta_{\text{pop}} - \gamma_{\text{src}} + 1}$. Such extremely UHE cosmic rays experience strong interactions during propagation, producing a large flux of light secondary cosmic rays with energies up to the Greisen-Zatsepin-Kuzmin (GZK) [84,85] limit. In combination with the remaining nondisintegrated component of heavy primaries, the predicted flux at Earth exhibits a large amount of mixing between the mass groups, which leads to strong intrinsic shower variance in excess of observations and an overall bad fit to the observed spectral shape.

The parameter space where a good fit to the measured UHECR spectrum and composition is achieved can be divided into two different regimes: one that runs approximately parallel to the boundary with $\beta_{\text{pop}} + \gamma_{\text{src}} \approx 4$–6 in the range $\gamma_{\text{src}} \in [-1, 0.5]$ and a second that is effectively degenerate in the population variance $\beta_{\text{pop}} \gtrsim 5$ with $\gamma_{\text{src}} \in [0, 1]$. The former is associated with a sub-EV maximum rigidity threshold R_0 and a heavy composition dominated by nitrogenlike nuclei with little contribution from lighter elements. The second regime allows for a lighter composition of up to $\sim 50\%$ protons/helium with $R_0 \sim 2$ EV. Only the second region is present in the scenario without fiducial scale shifts applied. In both regimes, sources are effectively identical and population variance of half a decade or more, i.e. $R_{\max}^{0.90}/R_0 > 5$, and

FIG. 5. Fit quality for the population model with broken-power-law distribution of maximum rigidities, marginalized onto $\beta_1 \times \beta_2$ space (the spectral index of the population spectrum below and beyond the break). Contours indicate the one (green) and three (red) sigma confidence intervals (2 d.o.f.). The white-shaded region denotes the parameter space where $R_{\max}^{0.90}/R_0 < 10$, i.e. where the spread in maximum rigidity is less than a decade for 90% of sources. The best fit is marked with a white cross. Parameters of potential source classes predicted based on their luminosity functions [Eq. (24)] are shown as black points. The allowed values of β_2 for blazars in the $R_{\max}(\Gamma)$ scenario [Eq. (19)] for the Hillas-constrained case and under the assumption that $\gamma_{\mathrm{src}} \geq 2$ are indicated on the left side.

$\beta_{\mathrm{pop}} \lesssim 2.4$, can be excluded at a confidence level above 6σ.[7] With EPOS-LHC, we obtain increased source variance at the best fit $\Delta\beta_{\mathrm{pop}} \approx -0.8$ but at the cost of a significantly reduced fit quality.

A statistically significant lower limit on the population variance cannot be established, and identical sources cannot be rejected.

B. Broken-power-law distribution of the maximum rigidity

We find that a broken-power-law distribution in $R_{\max}$ can fit the observed UHECR flux in the regime of highly nonidentical sources ($\beta_1 \gtrsim 1$) if
(I.a) the $R_{\max}$ distribution satisfies

$$\beta_2 \gtrsim \beta_1 + 3$$

as can be seen in Fig. 5 and

---

[7] A penalty factor S that corrects for the quality of the global best-fit point $\chi^2_{\min}$ is included in this estimate. We adopt the form $S^{-1} = \sqrt{\chi^2_{\min}/N_{\mathrm{d.o.f.}}}$ proposed in [86]. In essence, the penalty factor reduces the rejection strength of suboptimal fit points if the overall best fit is poor.

FIG. 6. Best-fit source spectral index γ_{src} (top) and break rigidity R_0 (bottom) as a function of β_1 and β_2 for the population model with a broken-power-law distribution of maximum rigidities. Best-fit confidence contours and source candidates are indicated as in Fig. 5. The structures in the upper left of the plots are artifacts from the limited resolution of our sampling grid and some degeneracy in the choice of $(R_0, \gamma_{\mathrm{src}})$ for a particular combination of (β_1, β_2).

(I.b)   the effective index of the rigidity spectra of the sources satisfies

$$\gamma_{\mathrm{pop}} = 1.22^{+0}_{-0.04},$$

as illustrated in Fig. 6.

This suggests that the effective population spectra $R^{-\gamma_{\mathrm{pop}}}$ must be moderately soft and the break must steepen the $R_{\max}$ distribution by at least $\times R_{\max}^{-3}$. Assuming reasonable source spectra, i.e. $\gamma_{\mathrm{src}} > 0 (> 1)[> 2]$, we can place an upper limit on the steepness of the subbreak $R_{\max}$ distribution of $\beta_1 \lesssim 2.2(1.2)[0.2]$.

If sources are in the regime of limited population variance ($\beta_1 \lesssim 1$) we find that they must satisfy (II.a)

$$\beta_2 \gtrsim 4.5$$

and
(II.b)

$$\gamma_{\rm src} = -0.6^{+1.2}_{-1.0},$$

consistent with the results for standard-candle sources. In summary, the key constraints that must be observed by potential source classes for 68% of realizations are

$$\gamma_{\rm src} = \begin{cases} 2.22^{+0}_{-0.04} & \text{for } \beta_1 \geq 1, \\ -0.6^{+1.2}_{-1.0} & \text{otherwise,} \end{cases} \quad (33)$$

$$\beta_2 \geq \begin{cases} \beta_1 + 3 & \text{for } \beta_1 \geq 1, \\ 4.5 & \text{otherwise.} \end{cases} \quad (34)$$

Our results clearly reflect the correlation of $\gamma_{\rm src}$ and β_1 expected from Eq. (B8). Large population variance (large β_1) is possible if individual source spectra are hard ($\gamma_{\rm src} \lesssim 1$). Pareto distributions ($\beta_2 \ll 1$) with sufficient flatness to produce substantial source variance ($\beta_2 \lesssim 3$) are disfavored at 4.7σ. All studied astrophysical source classes (Table II) are located in a region of the parameter space where "normal" (noninverted) spectral indices are preferred (Fig. 6) based on the values of β_1 and β_2 that we can infer from the studied luminosity functions. However, we found the predicted maximum rigidity distributions to be generally incompatible with the constraints of the UHECR fit. Only for Seyfert-like galaxies is the predicted $R_{\rm max}$ distribution above the break approximately compatible with the fit to the UHECR data.

The horizontal band at $\beta_2 \approx 6$ in Fig. 6 corresponds to a secondary family of viable solutions separate from the global minimum, with sub-EV break rigidity and harder injection spectra.

The best-fit parameters of the BPL and fiducial PL fit are compared in Table V. The more general, broken-power-law approach provides an improvement of $\Delta\chi^2 \approx 5.7$—which corresponds to a weak preference with respect to a single-power-law description at 2σ.

C. Redshift evolution of the source density

For simplicity, we have so far assumed the distribution of sources to be flat in redshift. However, the most probable source classes of UHECRs do not exhibit this behavior but have densities evolving as a function of redshift. A common parametrization of the evolution is given by

$$n(z) = \begin{cases} (1+z)^m & \text{for } m \leq 0, \\ (1+z)^m & \text{for } m > 0 \quad \text{and} \quad z < z_0, \\ z_0^m & \text{for } m > 0 \quad \text{and} \quad z_0 < z < z_{\rm max}, \\ 0 & \text{otherwise,} \end{cases}$$

$$(35)$$

which captures the general trends for the expected source classes: a power-law increase or decrease in density up to some break point and an approximate flattening above that. Positive redshift evolution ($m > 0$) is observed e.g. for active galactic nuclei [87] and gamma-ray bursts [45,88], and negative evolution for some BL Lac subclasses [89] and tidal disruption events [88,90,91]. Source densities following the star formation rate are approximately reproduced for $m = 3.4$ [92].

We study the effect of source density evolution on the allowed level of population variance by evaluating the fiducial model also for redshift evolutions of $m = -3, 3, 6$ with $z_0 = 1.5$ and $z_{\rm max} = 4$. Results are shown in Table IV.

Best agreement with observations is found for predominantly local sources ($m = -3$), and a continuous decrease in fit quality is identified for stronger density evolutions. The improved fit for small m is driven primarily by a better match of the observed composition, in particular $\langle X_{\rm max} \rangle$, but the difference in χ^2 only becomes large once $m > 3$. Redshift evolutions stronger than $m = 6$ could be excluded at more than 3σ based on their cosmogenic neutrino signature by future neutrino detectors such as GRAND-200k [93] or IceCube Gen2 [94].

We find a clear anticorrelation between source density evolution m and spectral index $\gamma_{\rm src}$, in agreement with previous studies, e.g. [10,11,69,95]. This is caused by the,

TABLE IV. Best-fit parameters for the fiducial model but with different source density redshift evolutions, where $n(z) \sim (1 + z)^m, z < 1.5$ [see Eq. (35)]. The second column ($m = 0$) is identical to the fiducial scenario presented in Table III. The injection fractions are given in descending order for p, He, N, Si and Fe. An asterisk indicates that the confidence interval extends to the edge of the scan range and the parameter is not properly constrained in that direction.

Redshift evolution m	-3	0	3	6
R_0 [EV]	$0.80^{+1.88}_{-0.16}$	$0.57^{+1.88}_{-0.11}$	$0.46^{+0.05}_{-0.09}$	$0.52^{+0.06}_{-0.05}$
$\beta_{\rm pop}$	$4.4^{+23.9}_{-0.5}$	$5.2^{+26.4*}_{-0.5}$	$6.46^{+0.36}_{-0.34}$	$6.46^{+0.36}_{-0.34}$
$\gamma_{\rm src}$	$0.2^{+0.8}_{-0.4}$	$-0.8^{+1.4}_{-0.5}$	$-2.0^{+0.4}_{-0.5}$	$-2.24^{+0.35}_{-0.18}$
$f_A^R[\%]$	$3.5^{+46.8}_{-3.5}$	$0^{+36.4}_{-0}$	$0^{+0.01}_{-0}$	0^{+0}_{-0}
	$8.7^{+49.8}_{-8.7}$	$0^{+51.3}_{-0}$	$2.6^{+17.0}_{-2.6}$	0^{+0}_{-0}
	$81.3^{+11.5}_{-46.7}$	$93.7^{+0.5}_{-53.5}$	$90.5^{+2.0}_{-16.2}$	$38.5^{+1.8}_{-15.7}$
	$1.7^{+3.7}_{-0.8}$	$0.3^{+7.7}_{-0.3}$	$0^{+0.9}_{-0}$	$53.0^{+16.2}_{-3.9}$
	$4.8^{+0.8}_{-2.8}$	$6.0^{+0.2}_{-3.8}$	$6.8^{+0.5}_{-1.3}$	$8.5^{+2.1}_{-0.5}$
$R_{\rm max}^{0.90}$ [R_0]	$1.97^{+0.22}_{-0.88}$	$1.72^{+0.13}_{-0.64}$	$1.53^{+0.04}_{-0.04}$	$1.53^{+0.04}_{-0.04}$
χ^2/d.o.f.	$37.3/26$	$40.6/26$	$42.5/26$	$68.9/26$

on average, larger source distance for stronger density evolutions and consequently increased interactions during propagation. Since interactions soften the spectrum, a harder injection spectrum is required at the sources. The same argument applies to the progressively heavier source composition at the best fit. For strong evolution, the viability of the β_{pop}-degenerate regime of the fiducial model is reduced and the $\beta_{pop} + \gamma_{src} \approx 4$ regime is preferred more strongly but shifted to harder source spectra $\gamma_{src} < 0$. Extremely identical sources are disfavored in this case because they would lead to a worse description of the observed spectral shape and an underestimation of the shower variance.

As established previously for the fiducial model, there exists an approximate boundary of $\beta_{pop} > -\gamma_{src} + 4$, which dictates that larger population variance requires softer source spectra. Local source distributions allow for softer spectra, and the source density redshift evolution and population variance are therefore positively correlated in the sense that smaller values of m allow for smaller values of β_{pop}.

To summarize, negative redshift evolutions of the source density provide many attractive benefits: (i) a quantitatively better fit to the observed UHECR spectrum and composition, (ii) lighter required injection composition, (iii) more natural spectral indices $\gamma_{src} > 0$, and (iv) a potentially higher, but still not very large, population variance. This makes classes of astrophysical objects with a negative redshift evolution, such as tidal disruption events [88,91] and high-spectral-peak BL Lacs [89], appealing as sources of ultrahigh-energy cosmic rays.

D. Redshift evolution of the maximum rigidity

In addition to the interactions with ambient photon fields, cosmic rays lose energy due to the adiabatic expansion of the Universe, with $E_{obs} = E_{inj}/(1+z)$. For a population of sources, this will lead to different effective maximum rigidities for sources at different distances and result in a naturally broadened population spectrum at Earth, even in the limit of identical sources.

We have previously assumed that the distribution of maximum rigidities $p(R_{max})$ does not depend on distance. However, most classes of astrophysical objects exhibit larger luminosities at higher redshifts [45,87,88]. If the maximum rigidity and luminosity of a cosmic-ray source are connected, as outlined in Sec. II D 2, then R_{max} should also evolve as a function of redshift. We study this scenario by evolving the starting point of the R_{max} distribution with redshift,

$$R_0(z) = R_0(1+z)^q, \qquad q \in \mathbb{R}. \qquad (36)$$

In the limit of $q = 0$, we obtain the default no-redshift-scaling case while for $q = 1$ adiabatic losses are exactly compensated, and sources would have the same effective maximum rigidity at all redshifts. Overcompensation
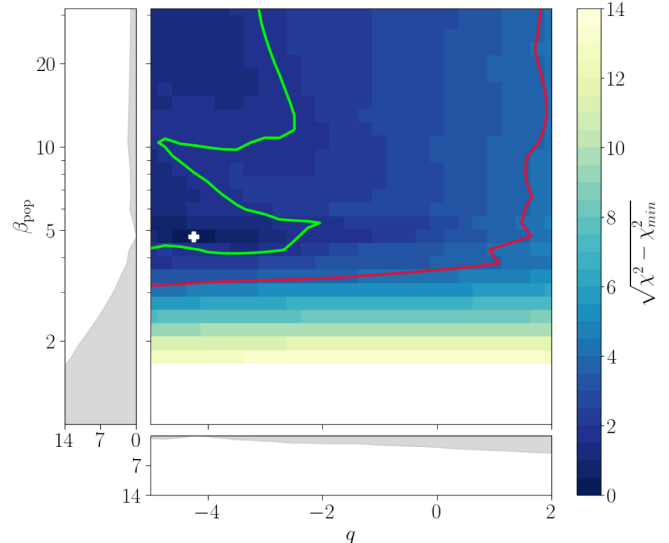

FIG. 7. Results of the source parameter scan for the population model with redshift evolution of the distribution of maximum rigidities marginalized onto $\beta_{pop} \times \gamma_{src}$ space. The agreement between prediction and Auger observations in terms of the χ^2 estimator is displayed with different color levels, and the contour lines indicate the one (green) and three (red) sigma confidence intervals for two degrees of freedom. The best fit is marked with a white cross.

$(q > 1)$ and even enhancement of local sources $(q < 0)$ are also possible.

We find that the cosmic-ray fit has only moderate sensitivity to the value of q, and no appreciable correlation with R_0, β_{pop} or γ_{src} is observed. Nevertheless, negative evolutions are preferred, with the best fit at $q = -4.3^{+1.0}_{-0.8*}$, and positive values of $q \geq 1$ excluded at 3σ confidence level. The difference is explained by a marginally better fit of the mean shower depth and a better description of the observed spectral shape, which is related to the stacking of contributions from different redshift shells.

Intuitively, the largest possible population rigidity variance should be allowed for a redshift scaling of $R_{max}(z) = R_{max}^{z=0} \cdot (1+z)$ as this would compensate the intrinsic broadening of the maximum rigidity termination via adiabatic energy losses. This expectation is not reflected in the results (Fig. 7), and we find a lower limit of $\beta_{pop}^{LL} \approx 4$ almost independent of q. A weak positive correlation of β_{pop}^{LL} and q can be observed, especially for the 3σ contour. This trend is related to the reduced fragmentation of heavy cosmic rays during propagation if the highest energies are reached only at the most local sources. As a consequence, negative evolutions of $R_{max}(z)$ allow for more extrinsic mixing of the mass groups due to nonidentical sources.

Perhaps the most tantalizing result of this scan is not the precise best fit but rather the realization that strongly positive rigidity-redshift scalings lead to an important multimessenger signature in the form of a large flux of
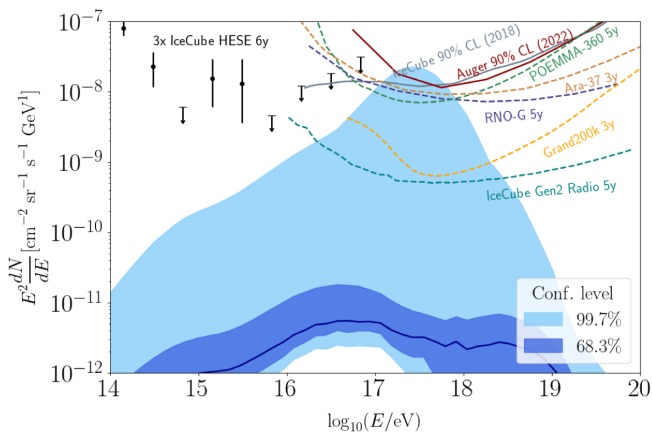
FIG. 8.   Predicted cosmogenic neutrino flux associated with the best fit (solid line) of the population model with redshift evolution of $p(R_{max})$. The shaded one and three sigma uncertainty bands correspond to the contours in Fig. 7. We show the observed IceCube HESE flux [67], upper limits from IceCube [68] and Auger [96], and predicted sensitivities of planned detectors [93,94,97,98] as a reference.

cosmogenic high-energy and ultrahigh-energy neutrinos (Fig. 8). If the evolution is strong, then the more distant, high-R_{max} sources are screened from our view in cosmic rays because of the interactions experienced during propagation. At the same time, these interactions produce a large flux of cosmogenic neutrinos that can reach us even from high redshifts. Around the peak at $E_\nu \approx 10^{17.4}$ eV more than 95% of the predicted neutrino flux is produced by UHECRs from sources at redshift $z > 1$. Based on this prediction, existing UHE limits of IceCube [68] and Auger [96] are able to constrain the redshift evolution of maximum rigidities to $q \lesssim 2$. However, we stress that this high neutrino flux is only obtained as the most extreme scenario within 3σ and only for a low number of specific realizations. With the increased sensitivity of future detectors, such as IceCube Gen2 and GRAND-200k, this upper limit can be reduced to $q \lesssim 1$ assuming a nondetection of UHE neutrinos.

The expected neutrino spectra differ substantially from predictions that are obtained without redshift scaling of the maximum rigidity both in shape and magnitude, especially for nonidentical sources and for strongly positive evolutions of R_{max}. The 99.7% upper limit (2 d.o.f.) in Fig. 8, with a peak in the neutrino flux between 0.1 and 1 EeV of up to $E^2 dN/dE \gtrsim 10^{-8}$ GeV cm^{-2} sr^{-1} s^{-1}, is obtained for approximately $R_0 = 1.8$ EV, $\beta_{pop} = 14.5$, $\gamma_{src} = 0.3$, $q = 2$, and injection fractions f_A^R: 0, 0.020, 0.875, 0.055, 0.050 (^{1}H ^{4}He, ^{14}N, ^{28}Si, ^{56}Fe). The large value of β_{pop} means that population variance is not an important ingredient for the large predicted neutrino flux in this scenario. The positive redshift evolution of R_{max} decreases the quality of the UHECR fit. For the same source parameters but no evolution ($q = 0$), and matching injection fractions, the fit improves by $\Delta\chi^2 = -7.9$.

We have verified that the predicted neutrino flux is in qualitative agreement with Refs. [69,95] if no redshift evolution of R_{max} and the same maximum source distance are assumed. Our upper limit of the cosmogenic neutrino flux is similar in magnitude to the flux predicted from interactions in the source environment in Ref. [17] but offset in energy by a factor of ~10.

Also visible in Fig. 8 is a new "shoulder" feature at ultrahigh neutrino energies beyond the classical CMB-induced peak. This feature is produced by cosmic rays with trans-GZK energies from the highest-energy tail of the population spectrum and is also present in the other scenarios we have studied. The extent and magnitude are linked to the strength of the UHECR tail and consequently to the amount of population variance.

The neutrino spectra in Fig. 8 are derived under the assumption of a source density that does not evolve as a function of distance. For sources that are more abundant in the local Universe the predicted flux is reduced while it is enhanced for most other realistic source classes (AGN [87] and GRB [45,88]).

E. Other variations of the source model

We have considered additional variations of the source model to study the impact on the allowed level

TABLE V.   Best-fit source spectral index γ_{src} and maximum rigidity variance β_{pop} plus corresponding χ^2 for different variations of the source model. These are (fd) the fiducial model, (bp) broken-power-law distribution of $p(R_{max})$, (zr) redshift evolution of $p(R_{max})$, (zn) redshift evolution of the source density, (zm) larger minimum source distance, (sc) superexponential source cutoff function, (fg) relative injection fractions similar to the composition observed for Galactic cosmic rays, and (ex) the extreme scenario that yields the largest amount of population variance with negative redshift evolution of the source density ($m = -3$) and Heaviside rigidity cutoff at the source. The best-fit values of the additional free parameters are $\beta_1 = 5.7^{+0.8}_{-0.4}$ and $\beta_2 = 23.1^{+8.5*}_{-10.8}$ for (bp), $q = -4.3^{+1.0}_{-0.8}$ for (zr), $\lambda = 5.4^{+1.7}_{-2.3}$ for (sc), and $\mu = 64.0^{+10.3}_{-8.8}$ for (fg). Confidence intervals that reach a limit of the scan range are marked with an asterisk.

Model	Parameter	β_{pop}	γ_{src}	χ^2
fd		$5.2^{+26.4*}_{-0.5}$	$-0.8^{+1.4}_{-0.5}$	40.4
bp	β_1, β_2	$18.4^{+8.5}_{-11.2}$	$-3.5^{+0.2}_{-0.8}$	34.7
zr	$q \in [-5, 2]$	$4.8^{+26.9*}_{-0.5}$	$-0.19^{+0.89}_{-0.18}$	33.7
zn	$m = -3$	$4.4^{+23.9}_{-0.5}$	$0.2^{+0.8}_{-0.4}$	37.3
	$m = 3$	$6.46^{+0.36}_{-0.34}$	$-2.0^{+0.4}_{-0.5*}$	42.5
	$m = 6$	$6.46^{+0.36}_{-0.34}$	$-2.24^{+0.35}_{-0.18}$	68.9
zm	$z_{min} = 0.01$	$29.9^{+1.7*}_{-25.5}$	$0.38^{+0.18}_{-1.22}$	46.2
sc	$\lambda \in [1, 50]$	$4.0^{+3.2}_{-0.4}$	$1.43^{+0.16}_{-0.16}$	33.6
fg	f_A^R	$4.9^{+0.5}_{-0.5}$	$0.73^{+0.16}_{-0.16}$	45.5
ex	Epos-LHC	$3.17^{+0.18}_{-0.17}$	$1.43^{+0.09}_{-0.09}$	40.6
	Sibyll2.3c	$3.5^{+0.6}_{-0.5}$	$1.69^{+0.09}_{-0.09}$	34.7

of population diversity in maximum rigidity (Table V). They are described briefly in the following. In all scenarios, a small but generally nonzero level of population variance on the order of $\beta_{pop} \sim 4$–6 is recovered at the best fit to Auger observations. The largest amount of source diversity —the most extreme case—is obtained for negative redshift evolution of the source density and Heaviside cutoff of the source spectra, which yields $\beta_{pop} \sim 3$–3.5 depending on the choice of hadronic interaction model.

1. Minimum source distance

Cosmic rays are attenuated during propagation depending on their source distance. UHECRs with energies around the cutoff and with the observed heavy composition are expected to reach us only from relatively local sources. To avoid artifacts in the simulations we have chosen $z_{min} = 10^{-3}$, or about 4.3 Mpc, as minimum source distance. Setting a larger minimum distance, i.e. 43 Mpc, we observe a decrease in fit quality for our fiducial model. This is because nearby sources contribute primarily at the highest energies. If these are removed, sources from larger distances must compensate for the loss in flux. However, for a Peters cycle progression of maximum rigidities with a preference for low maximum rigidities $\mathcal{O}(1\,\text{EeV})$ this compensation must come predominantly from heavier elements since only they can reach the required energies. Because of increased interaction due to the larger source distance, this also leads to the production of a substantial flux of lighter secondary cosmic rays and a stronger mixing of the mass groups—in contrast with observations. The tension can be partially mitigated when sources are essentially identical and the high-rigidity tail is very small. This shift to larger values of β_{pop} for the best fit is observed in our simulations; however, the viable range is not affected strongly, and the lower limit remains approximately the same.

2. Source cutoff function

Sources with an exponential UHE cutoff already include an intrinsic dispersion in the maximum rigidity of the produced cosmic rays even for a single source. This contribution is reduced for sharper-than-exponential cutoffs and becomes zero for a sudden, Heaviside-like limit. An increased level of population variance should therefore be expected for sources with a steeper cutoff function.

As proposed in Eqs. (6) and (13), a superexponential cutoff can be assumed with adjustable exponent λ_{cut}. Exactly Heaviside-like sources are obtained only for $\lambda_{cut} \to \infty$ but effectively the population spectra become very similar already for $\lambda_{cut} \gtrsim 2$. Beyond that point, the difference manifests mainly in the increasing sharpness of the break at R_0.

Resimulating the fiducial model for a range of exponents $\lambda_{cut} \in [1, 50]$, we find the global best fit at $\lambda_{cut} = 5.4^{+1.7}_{-2.3}$,
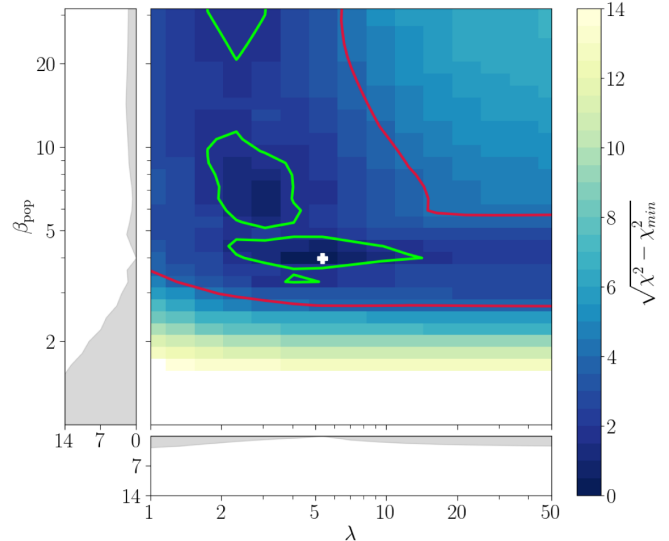

FIG. 9.   Results of the source parameter scan for the population model with superexponential source cutoff function, with exponent λ_{cut}, marginalized onto $\beta_{pop} \times \lambda_{cut}$ space. The surface plot shows the agreement between prediction and Auger observations in terms of the χ^2 estimator and the contour lines indicate the one (green) and three (red) sigma confidence interval for two degrees of freedom. The best fit is marked with a white cross.

which indicates effectively Heaviside-like sources. Overall the fit exhibits only moderate sensitivity to the precise shape of the cutoff except when it is close to an ordinary exponential (Fig. 9). The latter is disfavored at a level of 2.3σ. As expected from previous results, the population variance is poorly constrained for sources with exponential cutoff function, but even for close-to-Heaviside source cutoffs an upper limit cannot be placed—only at $\lambda_{cut} \gtrsim 8$ does a significant preference of intermediate diversity $\beta_{pop} \sim 4$ emerge. This reveals substantial dependence of the population variance on the precise shape of the spectrum at the break. We note that for approximately Heaviside-like sources the best-fit shifts to softer source spectra and hard spectra of $\gamma_{src} \lesssim 1$ are disfavored. This is in better agreement with the expectation from diffusive shock acceleration. The correlation between the sharpness of the cutoff and rigidity variance is not as strong as expected, and even sources with effectively instantaneous limit do not allow for diversities much greater than $\beta_{pop} \sim 3.5$.

3. Fixed injection composition

We investigate the scenario with injection fractions reflecting the composition observed for Galactic cosmic rays (GCRs). It is peculiar to note that an adequate fit of the UHECR data can be achieved with (near-)GCR-like composition if fractions are specified at the same energy [10,27,99]; however, this is not the case if fractions at the same rigidity are used. In the latter case, the abundance of heavy elements is insufficient to power the UHECR flux at

the highest energies, or in other words, the predicted composition at UHE is much lighter than indicated by observations.

We argue that rigidity fractions are the correct choice since the most relevant interactions for cosmic rays, such as electromagnetic reacceleration, magnetic horizon effects, and approximately also disintegration, are universal in rigidity and thus preserve the rigidity fractions but not the energy fractions. The fit is possible with fractions at the same energy since then the effective composition can be modified by changing the spectral index, due to $f_A^R = f_A^E Z^{-\gamma_{\rm src}+1}$.

We select the GCR composition at a fixed rigidity ($f_{\rm gal}^{\rm R}$: 0.794, 0.190, 0.013, 0.002, 0.001) [100] as our baseline scenario but allow for a free-floating rescaling of the metallicity, i.e. the abundance of elements heavier than helium, by a factor of $\mu \in [1, 100]$. With this model, the best agreement with observations is obtained for hard source spectra $\gamma_{\rm src} \approx 0.7$ and population variance of $\beta_{\rm pop} \approx 4.9$, which is similar to the source variance allowed in our fiducial scenario. At the best fit, a rescaling of the injection metallicity by a factor of approximately 60 is required, although values as low as $\mu \approx 20$ are allowed within the 3σ confidence interval.

V. CONCLUSION

We have performed the first systematic investigation of the allowed population variance in maximum UHECR rigidity. To this end, we have derived analytical expressions for the population spectrum of an ensemble of nonidentical UHECR sources, assuming a (broken-)power-law distribution of maximum rigidities $p(R_{\rm max}) \propto R_{\rm max}^{-\beta_{\rm pop}}$ and different choices of the spectral high-energy cutoff at the sources. For the first time, we have integrated this approach into a fit of the energy spectrum and composition data to quantify the constraints on source similarity from existing observations by the Pierre Auger Observatory.

If maximum rigidities are distributed according to a power law with a sudden start (Pareto distribution)—which appears as a suitable choice for several source candidates [e.g. AGN, blazars, tidal disruption events (TDEs)] based on the observed luminosity functions or under the assumption of power-law-distributed Lorentz factors—our results show that sources are required to be effectively identical if only Auger data at the nominal energy and composition scale are considered. After adjusting the measured mean shower depth and variance within systematic uncertainties to the favorable directions that result in the heaviest composition interpretation, we find that large yet finite values of $\beta_{\rm pop} \sim 5$ are preferred, corresponding to a dispersion in maximum rigidity of sources by a factor of approximately 2.

Increased levels of population variance up to $\beta_{\rm pop} \sim 3$–4 are possible for sources with sharp UHE cutoff and for source densities evolving negatively with redshift. Even then, maximum rigidities do not differ between sources by more than a factor of a few. In contrast, if sources are more

abundant at larger redshifts, they are required to be more identical because the preferred source spectrum becomes harder with redshift due to increased interactions during propagation. Since the population spectrum behaves as $\lim_{R\to\infty}(\phi_{\rm pop}) \propto R^{-\gamma_{\rm src}-\beta_{\rm pop}+1}$ a smaller source diversity (larger $\beta_{\rm pop}$) is required to limit the strength of the spectral UHE tail.

For some source classes (e.g. GRBs, blazars, Seyferts), the luminosity function motivates a broken-power-law distribution of maximum rigidities. In this scenario, the population variance can be large, driven by sources below the break rigidity R_0, provided the break is sharp and the spectral index of individual sources is sufficiently hard to counteract the variance introduced by the nonidentical sources. This requires hard spectral indices of $\gamma_{\rm src} \lesssim 1.2$ if the rigidity distribution below the break is softer than $\beta_1 \sim 1$. In addition, for any value of β_1, the $R_{\rm max}$ distribution must steepen at the break by at least $R_{\rm max}^{-3}$. For $\beta_1 \to -\infty$ we obtain the power-law scenario as an asymptotic limit, with $\gamma_{\rm src} \lesssim 1$ and $\beta_2 \gtrsim 4$.

We have derived the UHECR population spectra of plausible astrophysical source classes by connecting luminosity and maximum rigidity via the Lovelace-Blandford-Waxman relation [53–58], Eq. (24). For all proposed source classes, the preferred spectral index corresponding to their respective distribution $p(R_{\rm max}|\beta_1, \beta_2)$ is in the physically plausible range of $\gamma_{\rm src} = 0$–2 if they produce UHECRs with a maximum rigidity distribution which follows the one we have derived using their observed luminosity functions and Eq. (24). The predicted UHECR population spectra produced by blazars, tidal disruption events, and GRBs are inconsistent with the UHECR data within our formalism. Seyfert-like galaxies are the only investigated population (see Table II) with sufficiently steep postbreak slope to explain the required small variance at ultrahigh energies. However, a hard spectral index of $\gamma_{\rm src} \approx 0$–0.5 is necessary. The variance in maximum rigidity obtained using Eq. (24) represents a lower limit. Additional variance of the maximum rigidity is expected as a consequence of the distribution of other relevant source properties that we have not considered here, which will likely reduce this compatibility.

In summary, we have found that the maximum rigidity distribution of UHECR sources is remarkably narrow, necessitating nearly identical ("standard-candle") sources, or a sharp cutoff in the rigidity distribution of the UHECR source population. In the latter case, the low-rigidity tail exacerbates the need for hard injection spectra that has been exposed by prior studies which performed a combined fit of UHECR observations. Our results place strong constraints on the most plausible astrophysical source classes of UHECRs.

Alternatively, it is possible that exotic mechanisms limit the maximum rigidities of accelerators to the same value (e.g. [101]) or that the observed flux of UHECRs is dominated by a single local source. Such a single- or

few-source scenario seems however incompatible with the observed level of anisotropy of the cosmic-ray arrival directions at UHE unless deflections of cosmic rays in the Galactic and extragalactic magnetic fields are much larger than commonly expected. An analysis of the effect of cosmic variance is beyond the scope of this paper, but we comment that the fitted scenarios result in typical maximum rigidities that correspond to cosmic-ray energies below the onset of photonuclear interactions with the cosmic microwave background radiation. Thus the energy-loss lengths of nuclei are large, and the volume of UHECR sources contributing to the flux at Earth can be $\mathcal{O}(\mathrm{Gpc}^3)$.

APPENDIX A: TRANSFORMATION OF THE EMITTED FLUX

The apparent brightness of a highly relativistic source depends on the angle θ between the observer and the direction of motion and is affected by relativistic beaming (headlight effect) and the relativistic Doppler effect. However, for charged particles, we can assume that their direction of motion is isotropized after emission from the source, rendering geometrical beaming irrelevant. Only the Lorentz boost from the rest frame of the acceleration region to the observer frame must be considered. For sources with a flux cutoff f_{cut}, the differential flux within the jet frame is given by

$$\phi'(R') = \frac{\mathrm{d}^2 N'}{\mathrm{d}R'\mathrm{d}t'} = \phi'_0 R'^{-\gamma_{\mathrm{src}}} f_{\mathrm{cut}}(R'/R_0). \quad (A1)$$

To transform this flux into the observer frame the following transformations need to be taken into account

$$R = R'\Gamma^\alpha \quad \text{and} \quad t = t'\Gamma^\xi. \quad (A2)$$

Conservation of particle number implies $N = N'$. The first transformation is the boost in energy for particles,

with $\alpha = 1$ for particles accelerated in the jet frame and emitted isotropically[8] and $\alpha = 2$ for the espresso mechanism. The second transformation is due to time dilation, which also depends on the acceleration process. If production of UHECRs within the jet is considered, then the relativistic motion of the source region will stretch the observed time by a factor of Γ ($\xi = 1$). On the other hand, if an espressolike mechanism is assumed, where the jet merely reaccelerates a preexisting flux of cosmic rays $\mathrm{d}N/\mathrm{d}t$, then no dilation is expected, assuming that the rate of particles entering and exiting the jet is the same, i.e. $\mathrm{d}N/\mathrm{d}t|_{\mathrm{out}} = \mathrm{d}N/\mathrm{d}t|_{\mathrm{in}}$, and thus $\xi = 0$. The observed flux can then be written as

$$
\begin{aligned}
\phi(R) &= \frac{\mathrm{d}^2 N}{\mathrm{d}R\mathrm{d}t} = \frac{\mathrm{d}^2 N(R'(R))}{\mathrm{d}R'\mathrm{d}t'} \left| \frac{\mathrm{d}R'}{\mathrm{d}R} \right| \left| \frac{\mathrm{d}t'}{\mathrm{d}t} \right| \\
&= \phi'_0 R^{-\gamma_{\mathrm{src}}} \Gamma^{\alpha(\gamma_{\mathrm{src}}-1)-\xi} f_{\mathrm{cut}}\left(-\frac{R}{\Gamma^\alpha R_0} \right) \\
&= \phi'_0 R^{-\gamma_{\mathrm{src}}} \left(\frac{R_{\max}}{R_0} \right)^{\gamma_{\mathrm{src}}-1-\xi/\alpha} f_{\mathrm{cut}}\left(-\frac{R}{R_{\max}} \right), \quad (A3)
\end{aligned}
$$

where in the last step Eq. (19) was used. To evaluate the convolution of source spectra and $R_{\max}$ distributions, the product $\phi(R, R_{\max}) \times p(R_{\max})$ needs to be evaluated using the $R_{\max}$ distribution from Eq. (21). The resulting product can be rewritten in the "usual" form used in Sec. II C:

$$
\begin{aligned}
&\phi(R, R_{\max}) \times p(R_{\max}) \\
&= \phi_0 R^{-\gamma_{\mathrm{src}}} f_{\mathrm{cut}}\left(-\frac{R}{R_{\max}} \right) \frac{\beta_{\mathrm{pop}} - 1}{R_0} \left(\frac{R_{\max}}{R_0} \right)^{-\beta_{\mathrm{pop}}}, \quad (A4)
\end{aligned}
$$

with definitions

$$\phi_0 = \phi'_0 \frac{\eta - 1}{\eta + \alpha(1 - \gamma_{\mathrm{src}}) - \xi - 1} \quad (A5)$$

and

$$\beta_{\mathrm{pop}} = \frac{\eta - 1}{\alpha} + 2 - \gamma_{\mathrm{src}} + \xi/\alpha. \quad (A6)$$

Therefore, the same analytical forms derived in Sec. II C can be used in this case, but the interpretation of β_{pop} is more complex as it depends on several source properties.

APPENDIX B: BROKEN-POWER-LAW MAXIMUM RIGIDITY DISTRIBUTION

Source properties, e.g. luminosity (Sec. II D 2), often follow BPL distributions for some likely UHECR source

---

[8]For a general Lorentz boost of $\Gamma(1 - \beta \cos\theta)$ with isotropic emission angle θ the high-energy tail of the rigidity spectrum retains its spectral shape, and we concentrate on the simpler case of a boost by Γ.

classes rather than single PLs. A general broken-power-law distribution of maximum rigidities can be written as

$$p(R_{\max}) = \frac{R_0^{-1}}{C} \cdot \begin{cases} \left(\frac{R_{\max}}{R_0}\right)^{-\beta_1} & R_{\max} \leq R_0 \\ \left(\frac{R_{\max}}{R_0}\right)^{-\beta_2} & R_{\max} > R_0, \end{cases} \quad \text{(B1)}$$

with a break at R_0 and slope $R_{\max}^{-\beta_1}$ ($R_{\max}^{-\beta_2}$) below (above). Normalizability imposes $\beta_1 < 1$ and $\beta_2 > 1$. Under a physically more plausible scenario, with some minimum and maximum $R_{\max}$ ($R_{\max}^{\mathrm{LL}}/R_{\max}^{\mathrm{UL}}$) for the population of sources, these conditions can be relaxed and the normalization constant can be expressed as

$$C = \frac{1 - \left(\frac{R_{\max}^{\mathrm{LL}}}{R_0}\right)^{-\beta_1+1}}{1 - \beta_1} + \frac{1 - \left(\frac{R_{\max}^{\mathrm{UL}}}{R_0}\right)^{-\beta_2+1}}{\beta_2 - 1}. \quad \text{(B2)}$$

If $\beta_1 < 1$ and $\beta_2 > 1$, for $R_{\max}^{\mathrm{LL}} \to 0$ and $R_{\max}^{\mathrm{UL}} \to \infty$ this simplifies to

$$C = \frac{1}{1 - \beta_1} + \frac{1}{\beta_2 - 1}. \quad \text{(B3)}$$

Assuming source spectra with superexponential cutoff [Eq. (6)], the associated population spectrum reads

$$\phi_{\mathrm{pop}} = \frac{\phi_0}{C \cdot \lambda_{\mathrm{cut}}} R^{-\gamma_{\mathrm{src}}} \cdot [L + H]$$

$$L = \left(\frac{R}{R_0}\right)^{-\beta_1+1} \cdot \Gamma\left(\frac{\beta_1 - 1}{\lambda_{\mathrm{cut}}}, \left(\frac{R}{R_0}\right)^{\lambda_{\mathrm{cut}}}\right)$$

$$H = \left(\frac{R}{R_0}\right)^{-\beta_2+1} \cdot \gamma\left(\frac{\beta_2 - 1}{\lambda_{\mathrm{cut}}}, \left(\frac{R}{R_0}\right)^{\lambda_{\mathrm{cut}}}\right), \quad \text{(B4)}$$

with L the contribution from sources with $R_{\max}$ below the break at R_0 and H for sources above. For $\beta_1 \to -\infty$ a single power law is recovered. Because of the convergence properties of the incomplete gamma functions (Γ, γ),

$$\lim_{R/R_0 \to \infty} L = 0 \quad \text{and} \quad \lim_{R/R_0 \to 0} H = 0; \quad \text{(B5)}$$

i.e. in the limits of very small and very large rigidities, one of the terms dominates. Only in the vicinity of the break are their contributions of similar magnitude.

Equation (B4) suggests that the slope of the population spectrum at any rigidity is completely specified by a set of three parameters, with the most obvious choice $(\gamma_{\mathrm{src}}, \beta_1, \beta_2)$. However, an approximate description with only two parameters is possible, similar to the power-law scenario. The simplification is exact in the limit of very small and very large rigidities but not in the transition region where L and H have competitive levels. Two different cases can be identified depending on the value of β_1. The behavior in the high-rigidity limit is unaffected by the distribution below the break and is always $\phi_{\mathrm{pop}} \propto R^{-\gamma_{\mathrm{src}}-\beta_2+1}$.

(i) $\beta_1 \leq 1$.—Because the probability $p(R_{\max})$ increases only slowly for $R_{\max} \to 0$ it can be shown that $\lim_{R \to 0} \phi_{\mathrm{pop}} \propto R^{-\gamma_{\mathrm{src}}}$, suggesting that after interpretation $\beta_{\mathrm{pop}} = \beta_2$ we approximately retrieve the same population spectrum as for the single power law where $\beta_1 = -\infty$. The slope of the population spectrum can then be adequately described by the set of $(\gamma_{\mathrm{src}}, \beta_{\mathrm{pop}} = \beta_2)$.

(ii) $\beta_1 > 1$.—The contribution from sources below the break does not vanish and we obtain $\lim_{R \to 0} \phi_{\mathrm{pop}} \propto R^{-\gamma_{\mathrm{src}}-\beta_1+1}$. Initially, this does not appear compatible with a PL-like description; however, reinterpretation in terms of effective population spectral index $\gamma_{\mathrm{pop}} = \gamma_{\mathrm{src}} + \beta_1 - 1$ and effective $R_{\max}$ distribution $\beta_{\mathrm{pop}} = \beta_2 - \beta_1 + 1$ leads to the usual behavior

$$\lim_{R \to 0} \phi_{\mathrm{pop}} \propto R^{-\gamma_{\mathrm{pop}}}, \quad \text{(B6)}$$

$$\lim_{R \to \infty} \phi_{\mathrm{pop}} \propto R^{-\gamma_{\mathrm{pop}}-\beta_{\mathrm{pop}}+1}, \quad \text{(B7)}$$

with the difference that the distribution is now characterized by the redefined parameter set $(\gamma_{\mathrm{pop}}, \beta_{\mathrm{pop}})$. The above prescriptions can be used to interpret the fit results for a PL distribution given in Sec. IV for a population of sources with BPL($R_{\max}$). Yet, if not $\beta_1 \to -\infty$, the population variance predicted from Eq. (8) will underestimate the true variance since sources below the break are neglected (Fig. 10). All source classes proposed in Table II III. 2 belong to the $\beta_1 < 1$ category, enabling the simplified treatment.
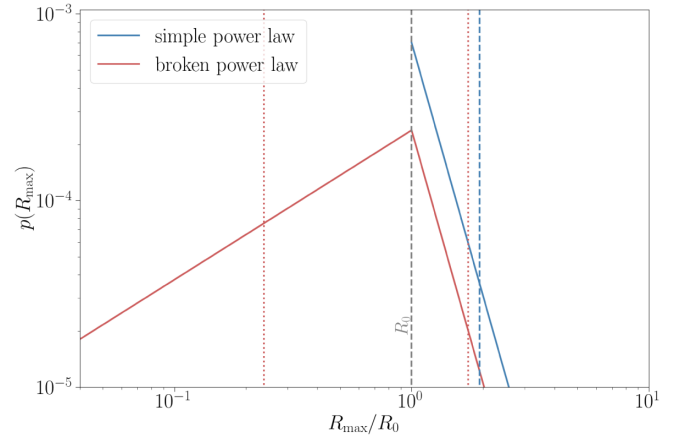

FIG. 10. Power-law (solid blue) and broken-power-law (solid red) distribution of maximum rigidities $p(R_{\max})$ with break or starting point at R_0, and $\gamma_{\mathrm{src}} = 2$, $\beta_1 = -0.8$, $\beta_2 = 4.5$. The one-sided 90% quantile of the PL (blue dashed line) and two-sided 90% quantile of the BPL (red dotted lines) are also displayed. In this scenario, the PL approach underestimates the population variance by a factor of ~3.8.

Although we do not predict steep subbreak distributions for any evaluated astrophysical source classes, it is still useful to study the scenario where $\beta_1 > 1$. The relevant parameters are now $(\gamma_{\mathrm{pop}}, \beta_{\mathrm{pop}})$, defined as

$$\text{(a)} \quad \gamma_{\mathrm{pop}} = \gamma_{\mathrm{src}} + \beta_1 - 1, \qquad \text{(B8)}$$

$$\text{(b)} \quad \beta_{\mathrm{pop}} = \beta_2 - \beta_1 + 1. \qquad \text{(B9)}$$

Solutions of this system are degenerate and different choices of $(\gamma_{\mathrm{src}}, \beta_1, \beta_2)$ can lead to the same population spectrum.[9] One of the parameters must be fixed with additional information to break the degeneracy. This is a remarkable finding—a similar population spectrum can be

---

[9]Except for the cutoff shape at R_0. Combinations of steep source distributions and hard source spectra will lead to sharper cutoffs than more identical sources with softer spectra.

achieved for highly identical sources with softer spectral index and for diverse sources with harder spectral index. Therefore, the distribution below the cutoff can be steep and sources very diverse, provided individual sources have ultrahard spectra so that Eq. (B8) remains fulfilled. If this condition is satisfied and the break at R_0 is sufficiently strong, then the UHECR flux is dominated by sources very close to the break at R_0, explaining the apparently low population variance. Sources further below the break still contribute to the flux at lower rigidities by modifying the population spectrum as $\phi_{\mathrm{pop}} \propto R^{-\gamma_{\mathrm{src}}} \rightarrow R^{-\gamma_{\mathrm{src}}-\beta_1+1}$ if $\beta_1 > 1$. For flatter subbreak distributions, their contribution is approximately negligible except close to the break. This suggests that the sources of UHECRs can appear very similar even if the underlying population is diverse, provided the UHE termination of the R_{max} distribution is sufficiently sharp, and the distribution before the cutoff is not too steep after taking into account the hardness of individual source spectra.

[1] L. A. Anchordoqui, Phys. Rep. **801**, 1 (2019).
[2] R. Alves Batista et al., Front. Astron. Space Sci. **6**, 23 (2019).
[3] A. di Matteo et al. (Telescope Array and Pierre Auger Collaborations), Proc. Sci. ICRC2021 (**2021**) 308 [arXiv:2111.12366].
[4] D. Allard, E. Parizot, and A. V. Olinto, Astropart. Phys. **27**, 61 (2007).
[5] D. Hooper, S. Sarkar, and A. M. Taylor, Astropart. Phys. **27**, 199 (2007).
[6] D. Allard, A. V. Olinto, and E. Parizot, Astron. Astrophys. **473**, 59 (2007).
[7] D. Allard, N. G. Busca, G. Decerprit, A. V. Olinto, and E. Parizot, J. Cosmol. Astropart. Phys. 10 (2008) 033.
[8] N. Globus, D. Allard, R. Mochkovitch, and E. Parizot, Mon. Not. R. Astron. Soc. **451**, 751 (2015).
[9] N. Globus, D. Allard, and E. Parizot, Phys. Rev. D **92**, 021302 (2015).
[10] M. Unger, G. R. Farrar, and L. A. Anchordoqui, Phys. Rev. D **92**, 123001 (2015).
[11] A. Aab et al. (Pierre Auger Collaboration), J. Cosmol. Astropart. Phys. 04 (2017) 038; 03 (2018) E02.
[12] K. Fang and K. Murase, Phys. Lett. **14**, 396 (2018); Nat. Phys. **14**, 396 (2018).
[13] M. Kachelrieß, O. Kalashev, S. Ostapchenko, and D. V. Semikoz, Phys. Rev. D **96**, 083006 (2017).
[14] D. Boncioli, D. Biehl, and W. Winter, Astrophys. J. **872**, 110 (2019).
[15] M. S. Muzio, M. Unger, and G. R. Farrar, Phys. Rev. D **100**, 103008 (2019).
[16] J. Heinze, D. Biehl, A. Fedynitch, D. Boncioli, A. Rudolph, and W. Winter, Mon. Not. R. Astron. Soc. **498**, 5990 (2020).

[17] M. S. Muzio, G. R. Farrar, and M. Unger, Phys. Rev. D **105**, 023022 (2022).
[18] P. Abreu et al. (Pierre Auger Collaboration), Proc. Sci. ICRC2021 (**2021**) 311.
[19] D. Bergman (Telescope Array Collaboration), Proc. Sci. ICRC2021 (**2021**) 338.
[20] A. A. Halim et al. (Pierre Auger Collaboration), arXiv:2211.02857.
[21] B. Peters, Nuovo Cimento (1955–1965) **22**, 800 (1961).
[22] T. K. Gaisser, R. Engel, and E. Resconi, Cosmic Rays and Particle Physics (Cambridge University Press, Cambridge, England, 2016), 2nd ed.
[23] K. V. Ptitsyna and S. V. Troitsky, Phys. Usp. **53**, 691 (2010).
[24] M. Ahlers, L. A. Anchordoqui, and A. M. Taylor, Phys. Rev. D **87**, 023004 (2013).
[25] B. Eichmann, J. P. Rachen, L. Merten, A. van Vliet, and J. Becker Tjus, J. Cosmol. Astropart. Phys. 02 (2018) 036.
[26] B. Eichmann, M. Kachelrieß, and F. Oikonomou, J. Cosmol. Astropart. Phys. 07 (2022) 006.
[27] X. Rodrigues, J. Heinze, A. Palladino, A. van Vliet, and W. Winter, Phys. Rev. Lett. **126**, 191101 (2021).
[28] S. Das, S. Razzaque, and N. Gupta, Eur. Phys. J. C **81**, 59 (2021).
[29] S. Mollerach and E. Roulet, Phys. Rev. D **101**, 103024 (2020).
[30] J. H. Matthews and A. M. Taylor, Mon. Not. R. Astron. Soc. **503**, 5948 (2021).
[31] P. Lipari, Astropart. Phys. **125**, 102507 (2021).
[32] Q. Yuan, B. Zhang, and X.-J. Bi, Phys. Rev. D **84**, 043002 (2011).
[33] M. Kachelriess and D. V. Semikoz, Phys. Lett. B **634**, 143 (2006).

[34] M. Shibata, Y. Katayose, J. Huang, and D. Chen, Astrophys. J. **716**, 1076 (2010).

[35] A. R. Bell, Mon. Not. R. Astron. Soc. **182**, 147 (1978).

[36] A. R. Bell, Mon. Not. R. Astron. Soc. **182**, 443 (1978).

[37] R. J. Protheroe and T. Stanev, Astropart. Phys. **10**, 185 (1999).

[38] R. J. Protheroe, Astropart. Phys. **21**, 415 (2004).

[39] V. N. Zirakashvili and F. Aharonian, Astron. Astrophys. **465**, 695 (2007).

[40] M. L. Lister et al., Astrophys. J. **874**, 43 (2019).

[41] M. Ajello et al., Astrophys. J. **699**, 603 (2009).

[42] L. Marcotulli et al. (BASS Collaboration), Astrophys. J. **940**, 77 (2022).

[43] S. van Velzen, Astrophys. J. **852**, 72 (2018).

[44] Z. Lin, N. Jiang, X. Kong, S. Huang, Z. Lin, J. Zhu, and Y. Wang, Astrophys. J. Lett. **939**, L33 (2022).

[45] D. Wanderman and T. Piran, Mon. Not. R. Astron. Soc. **406**, 1944 (2010).

[46] Y. Ueda, M. Akiyama, G. Hasinger, T. Miyaji, and M. G. Watson, Astrophys. J. **786**, 104 (2014).

[47] P. Saikia, E. Körding, and H. Falcke, Mon. Not. R. Astron. Soc. **461**, 297 (2016).

[48] A. M. Hillas, Annu. Rev. Astron. Astrophys. **22**, 425 (1984).

[49] D. Caprioli, Astrophys. J. Lett. **811**, L38 (2015).

[50] R. Mbarek and D. Caprioli, Astrophys. J. **886**, 8 (2019).

[51] R. Mbarek and D. Caprioli, Astrophys. J. **921**, 85 (2021).

[52] M. L. Lister and A. P. Marscher, Astrophys. J. **476**, 572 (1997).

[53] R. V. E. Lovelace, Nature (London) **262**, 649 (1976).

[54] E. Waxman, Phys. Rev. Lett. **75**, 386 (1995).

[55] E. Waxman, ICTP Lect. Notes Ser. **4**, 309 (2001).

[56] R. D. Blandford, Phys. Scr. T **85**, 191 (2000).

[57] M. Lemoine and E. Waxman, J. Cosmol. Astropart. Phys. 11 (2009) 009.

[58] M. Kachelriess, Proc. Sci. ICRC2021 (**2022**) 018 [arXiv:2201.04535].

[59] F. M. Rieger, Universe **8**, 607 (2022).

[60] F. Santoro, C. Tadhunter, D. Baron, R. Morganti, and J. Holt, Astron. Astrophys. **644**, A54 (2020).

[61] A. Aab et al. (Pierre Auger Collaboration), Phys. Rev. D **102**, 062005 (2020).

[62] A. Aab et al. (Pierre Auger Collaboration), Phys. Rev. D **90**, 122005 (2014).

[63] A. Yushkov (Auger Collaboration), Proc. Sci. ICRC2019 (**2020**) 482.

[64] K.-H. Kampert and M. Unger, Astropart. Phys. **35**, 660 (2012).

[65] R. Alves Batista et al., J. Cosmol. Astropart. Phys. 05 (2016) 038.

[66] M. Ackermann et al. (Fermi-LAT Collaboration), Astrophys. J. **799**, 86 (2015).

[67] C. Kopper (IceCube Collaboration), Proc. Sci. ICRC2017 (**2018**) 981.

[68] M. G. Aartsen et al. (IceCube Collaboration), Phys. Rev. D **98**, 062003 (2018).

[69] R. Alves Batista, R. M. de Almeida, B. Lago, and K. Kotera, J. Cosmol. Astropart. Phys. 01 (2019) 002.

[70] R. Alves Batista, D. Boncioli, A. di Matteo, A. van Vliet, and D. Walz, J. Cosmol. Astropart. Phys. 10 (2015) 063.

[71] R. C. Gilmore, R. S. Somerville, J. R. Primack, and A. Domínguez, Mon. Not. R. Astron. Soc. **422**, 3189 (2012).

[72] R. Aloisio and V. Berezinsky, Astrophys. J. **612**, 900 (2004).

[73] J. M. González, S. Mollerach, and E. Roulet, Phys. Rev. D **104**, 063005 (2021).

[74] S. Mollerach and E. Roulet, J. Cosmol. Astropart. Phys. 10 (2013) 013.

[75] N. Globus, D. Allard, and E. Parizot, Astron. Astrophys. **479**, 97 (2008).

[76] D. Wittkowski, Proc. Sci. ICRC2017 (**2017**) 563.

[77] P. Abreu et al. (Pierre Auger Collaboration), J. Cosmol. Astropart. Phys. 02 (2013) 026.

[78] A. M. Hillas, J. Phys. G **31**, R95 (2005).

[79] S. Baker and R. D. Cousins, Nucl. Instrum. Methods **221**, 437 (1984).

[80] B. Dawson (Pierre Auger Collaboration), Proc. Sci. ICRC2019 (**2020**) 231.

[81] F. Riehn, H. P. Dembinski, R. Engel, A. Fedynitch, T. K. Gaisser, and T. Stanev, Proc. Sci. ICRC2017 (**2018**) 301 [arXiv:1709.07227].

[82] T. Pierog, I. Karpenko, J. M. Katzy, E. Yatsenko, and K. Werner, Phys. Rev. C **92**, 034906 (2015).

[83] V. Verzi, Proc. Sci. ICRC2019 (**2019**) 450.

[84] K. Greisen, Phys. Rev. Lett. **16**, 748 (1966).

[85] G. T. Zatsepin and V. A. Kuzmin, JETP Lett. **4**, 78 (1966).

[86] A. H. Rosenfeld, Annu. Rev. Nucl. Part. Sci. **25**, 555 (1975).

[87] G. Hasinger, T. Miyaji, and M. Schmidt, Astron. Astrophys. **441**, 417 (2005).

[88] H. Sun, B. Zhang, and Z. Li, Astrophys. J. **812**, 33 (2015).

[89] M. Ajello et al., Astrophys. J. **780**, 73 (2014).

[90] C. Guépin, K. Kotera, E. Barausse, K. Fang, and K. Murase, Astron. Astrophys. **616**, A179 (2018); **636**, C3(E) (2020).

[91] C. S. Kochanek, Mon. Not. R. Astron. Soc. **461**, 371 (2016).

[92] A. M. Hopkins and J. F. Beacom, Astrophys. J. **651**, 142 (2006).

[93] J. Álvarez-Muñiz et al. (GRAND Collaboration), Sci. China Phys. Mech. Astron. **63**, 219501 (2020).

[94] M. G. Aartsen et al. (IceCube Collaboration), arXiv:1911.02561.

[95] J. Heinze, A. Fedynitch, D. Boncioli, and W. Winter, Astrophys. J. **873**, 88 (2019).

[96] F. Pedreira (Pierre Auger Collaboration), Proc. Sci. ICRC2019 (**2021**) 979.

[97] P. Allison et al. (ARA Collaboration), Phys. Rev. D **93**, 082003 (2016).

[98] A. L. Cummings, R. Aloisio, and J. F. Krizmanic, Phys. Rev. D **103**, 043017 (2021).

[99] S. S. Kimura, K. Murase, and B. T. Zhang, Phys. Rev. D **97**, 023026 (2018).

[100] P. A. Zyla et al. (Particle Data Group), Prog. Theor. Exp. Phys. **2020**, 083C01 (2020).

[101] L. A. Anchordoqui, Phys. Rev. D **106**, 116022 (2022).